INVESTIGATION OF SKY RADIANCE IN TROPICAL CLIMATE OF THAILAND

By

MR. Worapan KANCHANACHAT

A Thesis Submitted in Partial Fulfillment of the Requirements

for Doctor of Philosophy PHYSICS

Department of PHYSICS

Silpakorn University

Academic Year 2024

การศึกษารังสีกระจายจากส่วนต่าง ๆ ของท้องฟ้าในสภาพภูมิอากาศแบบเขตร้อนของประเทศไทย

โดย
นายวรพันธุ์ การชนะชาติ

วิทยานิพนธ์นี้เป็นส่วนหนึ่งของการศึกษาตามหลักสูตรปรัชญาดุษฎีบัณฑิต
สาขาวิชาฟิสิกส์ แบบ 1.1
ภาควิชาฟิสิกส์
มหาวิทยาลัยศิลปากร
ปีการศึกษา 2567

INVESTIGATION OF SKY RADIANCE IN TROPICAL CLIMATE OF THAILAND

By

MR. Worapan KANCHANACHAT

A Thesis Submitted in Partial Fulfillment of the Requirements

for Doctor of Philosophy PHYSICS

Department of PHYSICS

Academic Year 2024

Title	Investigation of sky radiance in tropical climate of Thailand
By	MR. Worapan KANCHANACHAT
Field of Study	PHYSICS
Advisor	Assistant Professor Dr. Itsara Masiri
Co advisor	Professor Dr. Serm Janjai

Faculty of Science, Silpakorn University in Partial Fulfillment of the Requirements for the Doctor of Philosophy

.....Dean of Faculty of Science
(Assistant Professor Dr. Narong Chimpalee)

Approved by

.....Chair person
(Associate Professor Dr. Wilawan Kamharn)

.....Advisor
(Assistant Professor Dr. Itsara Masiri)

.....Co advisor
(Professor Dr. Serm Janjai)

.....Committee
(Associate Professor Dr. Sumaman Buntoung)

.....Committee
(Assistant Professor Dr. Korntip Tohsing)

.....Committee
(Assistant Professor Dr. Rungrat Wattan)

มหาวิทยาลัยศิลปากร

650730009 : Major PHYSICS
Keyword : Empirical model; Relative sky radiance; Zenith sky radiance; Tropical climate

MR. Worapan KANCHANACHAT : Investigation of sky radiance in tropical climate of Thailand Thesis advisor : Assistant Professor Dr. Itsara Masiri

This study aims to develop two empirical models related to sky radiance in the tropical climate of Thailand. The first objective is to create an empirical model for calculating relative sky radiance under various sky and climatic conditions. The model identifies sky conditions through a cloud index derived from geostationary satellite imagery and employs empirical adjustable coefficients established from five years of averaged sky radiance data at Nakhon Pathom station. Validation using measurement data from four main regions: Chiang Mai, Ubon Ratchathani, Songkhla, and Nakhon Pathom, under clear, intermediate and overcast sky conditions showed that the model achieved root mean square error (RMSE) values of approximately 30% across the different conditions. Although the coefficients were derived from a single station, comparisons across regions with diverse climatic characteristics confirmed the broader applicability of the model. The second objective is to develop an empirical model for calculating hourly zenith sky radiance as a function of solar altitude under clear sky conditions, focusing on a case study of Chiang Mai and Nakhon Pathom. Hourly zenith sky radiance measurement data from the Nakhon Pathom station were used for model development. Data collected at both Chiang Mai and Nakhon Pathom stations were employed to validate the accuracy of the model. The results demonstrated reasonable accuracy, with an RMSE of 30.17% and a mean bias error (MBE) of 7.48%.

ACKNOWLEDGEMENTS

First and foremost, I would like to express my heartfelt gratitude to everyone who supported me throughout this journey to obtain my Ph.D. degree. Without their encouragement, help, and patience, this achievement would not have been possible.

I am particularly grateful to my advisor, Asst. Prof. Dr. Itsara Masiri, for his invaluable guidance, thoughtful suggestions, and constant support during every stage of this research. His expertise, patience, and encouragement have been indispensable to my growth as a researcher. I am truly honored to have had the opportunity to work under his mentorship.

I am also deeply indebted to my Co advisor, Prof. Dr. Serm Janjai, whose funding support has been crucial to my academic development. His introduction to the field of solar radiation has significantly shaped my research direction, and I am immensely thankful for his insights and encouragement throughout this journey.

I would like to extend my sincere thanks to my thesis committee and external examiner for their insightful comments, constructive feedback, and valuable suggestions that helped refine and improve my work. Their expert guidance has been vital in shaping the final version of this thesis.

I am also deeply grateful to the professors, staff, and classmates in the Solar Energy Research Laboratory, Department of Physics, Faculty of Science, Silpakorn University. Their collaboration, technical assistance, and moral support have played an essential role in the completion of my research.

Finally, I would like to express my deepest appreciation to my family. Their unconditional love, support, and constant care have been my greatest source of strength throughout this entire process. Their belief in me kept me motivated, and I will be forever grateful for their sacrifices and encouragement.

Worapan KANCHANACHAT

TABLE OF CONTENTS

Page

LIST OF TABLES

Page

LIST OF FIGURES

Page

Chapter 1

Introduction

1.1 Rational of the study

In urban environments, photovoltaic (PV) panels are often installed on vertical surfaces or building facades (de Simón-Martín et al., 2017). This approach is particularly useful in densely built areas where roof space for horizontal installation is limited. Despite its advantages, utilizing solar energy in urban settings presents challenges. High-rise buildings in densely populated areas can obstruct solar irradiance, reducing PV panel efficiency. To address these challenges, urban planners and architects must carefully design buildings to optimize solar irradiance access. Generally, the presence of obstacles causes direct solar irradiance to scatter, increasing diffuse solar irradiance (Norton, 2012). This scattered irradiance, which reaches surfaces from various directions, is often the dominant form of solar irradiance in cities. The distribution of diffuse solar irradiance over the sky dome or sky radiance can be obtained using a sky scanner (Li and Lam, 2007), an instrument that measures sky radiance (R) and sky luminance (L). Both values are also known as absolute values. However, sky scanners are expensive and impractical for widespread deployment. Over the last decade, researchers have focused on developing models to calculate L for natural daylight planning in the visible light (VIS) wavelength. To establish a standard model, the CIE (Commission Internationale de l'Éclairage) adopted 15 types of skies, known as the 15 CIE standard sky models, to calculate L relative to zenith sky luminance (L_z), also referred to as relative sky luminance (L / L_z) (CIE, 2003).

Silicon-based PV panels are sensitive to a broad range of wavelengths, specifically from 300 to 1200 nanometers. This range includes ultraviolet (UV), VIS, and near-infrared (NIR) wavelength (Goswami, 2022). However, the widely used CIE standard sky model for L / L_z commonly employed to estimate solar irradiance for PV applications (Li et al., 2016) is fundamentally based on VIS measurements and does not account for the UV and NIR components that are also critical for PV energy

conversion. As a result, relying on CIE standard sky model can introduce significant uncertainties in estimating the actual power output of PV systems (Hess, 2014). Therefore, this study focuses on investigating sky radiance across the spectral range relevant to PV sensitivity in both zenith sky radiance (R_z) and relative sky radiance (R / R_z) in the tropical climate of Thailand.

1.2 Objectives

1) To develop an empirical model for calculating R / R_z under different sky and climate conditions in the tropical climate of Thailand using geostationary satellite data.
2) To develop an empirical model for calculating R_z under clear sky conditions: A case study of Chiang Mai and Nakhon Pathom, Thailand.

1.3 Structure of the thesis

This thesis is organized into five chapters. Chapter 1 provides the rationale for the study, outlining its main motivation and objectives. Chapter 2 presents relevant theories and a literature review of related studies. Chapter 3 details the development of a method for calculating R / R_z under different sky and climate conditions in the tropical environment of Thailand using geostationary satellite imagery. Chapter 4 demonstrates the method for calculating R_z under clear sky conditions, with a focus on case studies in Chiang Mai and Nakhon Pathom. Finally, Chapter 5 presents the conclusion of the study.

Chapter 2

Theory and literature review

Before conducting research on sky radiance modeling, it is essential to have a solid understanding of the theoretical and conceptual frameworks of solar radiation, which are necessary for fully comprehending the research. Therefore, this chapter presents the related theories and a literature review as follows.

2.1 Solar radiation

Nuclear fusion in the core of the Sun occurs under extreme temperatures and pressures, where hydrogen nuclei fuse to form helium (Tiwari et al., 2016). According to thermodynamic principles, this process releases vast amounts of energy, primarily as high-energy gamma rays. The core of the Sun reaches approximately 15 million degrees Celsius, providing the necessary conditions for fusion. The gamma rays produced in the core do not escape immediately. Instead, they undergo a prolonged journey outward, interacting with surrounding plasma through Compton scattering, absorption, and re-emission. These interactions gradually reduce the energy of gamma rays, converting them into lower-energy photons such as X-rays, ultraviolet light, visible light, infrared radiation, and radio waves (George et al., 2017). The transfer and transformation of energy within the Sun can take thousands to millions of years, as photons are repeatedly scattered and absorbed before reaching the outer layers. Once at the surface of the Sun, these photons are emitted as solar radiation, covering a broad spectrum of electromagnetic waves. This energy is then released into space at the speed of light (approximately 3×10^{8} m/s), taking approximately 8 minutes to reach Earth's atmosphere. Solar radiation serves as the primary energy source for Earth, playing a vital role in climate regulation and sustaining life.

2.2 Definitions

1) Radiance: the amount of solar energy emitted in a specific direction per unit area within a given solid angle is known as radiance. Radiance is measured in watts per square meter per steradian ($W/m^2 \cdot sr$) and encompasses the entire solar energy spectrum.

2) Irradiance: the integral of the radiance over a sky dome is known as irradiance. Instantaneous irradiance received per unit area on a surface is expressed in watts per square meter (W/m^2), whereas the accumulation of irradiance over a specified period is typically reported in megajoules per square meter (MJ/m^2).

3) Radiation: the overall spectrum of solar energy emitted by the Sun, encompassing all wavelengths of solar irradiance.

2.3 Solar radiation at the Earth's atmosphere

The Sun radiates an immense amount of energy, with an average solar constant of approximately 1367 W/m^2 (Tiwari et al., 2016) at the Earth's outer atmosphere. However, only a fraction of this energy reaches the Earth's surface due to various interactions with the atmosphere. These interactions (including scattering, absorption, and reflection) (Norton, 2012) significantly modify the amount and intensity of solar irradiance that ultimately reaches the ground. The Earth's atmosphere plays a crucial role in shaping the characteristics of solar irradiance. The portion of solar irradiance that reaches the Earth's surface directly is known as direct solar irradiance, whereas the scattered component is referred to as diffuse solar irradiance. The sum of both components is global solar irradiance.

In urban environments, the presence of obstacles like buildings, trees, and other structures, combined with atmospheric factors such as clouds and aerosols, causes direct solar irradiance to scatter, resulting in an increase in diffuse solar irradiance (Norton, 2012). This scattered irradiance, which reaches surfaces from various

directions, is often the dominant form of irradiance in cities. The distribution of diffuse solar irradiance over the sky dome is also known as sky radiance.

2.4 Solar irradiance on a surface with an inclination angle

The limited availability of rooftop space in modern buildings has led to the increased adoption of vertical PV panel installations (Li and Lam, 2004). With urban areas experiencing rapid development and high-rise structures becoming more prevalent, rooftop surfaces alone are often insufficient to meet the energy demands of buildings. As a result, Building-Integrated Photovoltaic (BIPV) systems, including PV facades and solar windows, have emerged as a viable solution to enhance energy generation while seamlessly integrating into architectural designs. To calculate global solar irradiance incident on a PV panel ($I_{\beta G}$, in W/m^2) with an inclination angle of β (degree), it includes three components: direct solar irradiance, the distribution of diffuse solar irradiance over the sky dome or sky radiance, and the reflected irradiance component. This can be expressed as (Li and Lam, 2004; Muneer, 2007):

$$I_{\beta G} = I_{\beta B} + I_{\beta D} + I_{\beta R} \quad (1.1)$$

where $I_{\beta B}$ is the direct solar irradiance with an inclination angle of β (W/m^2), $I_{\beta D}$ is the distribution of diffuse solar irradiance over the sky dome (W/m^2) with an inclination angle of β, and $I_{\beta R}$ is the ground-reflected irradiance (W/m^2) with an inclination angle of β. Calculation of direct solar irradiance is straightforward, given the position of the sun and inclination of the surface which are shown in many studies (Drif et al., 2008). For calculating the ground-reflected irradiance, it is assumed that the inclined surface receives the global solar irradiance reflected isotopically from the ground surface (Drif et al., 2008). Thus, $I_{\beta R}$ would depend on β and the average ground reflectivity. The $I_{\beta B}$ and $I_{\beta R}$ can be calculated as:

$$I_{\beta B} = \frac{I_{HB}}{sin(\alpha_s)}\left[sin(\alpha_s)cos(\beta) + cos(\alpha_s)cos(\beta)cos(\varphi_s - \varphi_N)\right] \quad (2.2)$$

$$I_{HB} = I_{HG} - I_{HD} \quad (2.3)$$

$$I_{\beta R} = \rho I_{HG}(1 - cos(\beta))/2 \quad (2.4)$$

where I_{HB} is the direct solar irradiance on horizontal surface (W/m^2), I_{HG} is the global solar irradiance on horizontal surface (W/m^2), α_s is the solar altitude angle (degree), φ_s is the solar azimuth angle (degree), φ_N is the azimuth angle of the normal of the surface (degree), and ρ is the reflectance of ground surface, which was considered to 0.2 (Drif et al., 2008).

The key challenge is calculating $I_{\beta D}$. Because aerosols in the atmosphere strongly scatter light forward, the radiance from the sky dome can vary significantly in different directions (Li and Lam, 2004). As a result, $I_{\beta D}$ is highly uneven and difficult to model, especially in non-overcast conditions. The amount of diffuse solar irradiance depends on both the intensity and distribution of radiance from different parts of the sky. Theoretically, the irradiance on an inclined plane contributed by a small section of the sky is given by:

$$\delta I_{\beta D} = R_{\alpha\varphi} cos(\sigma)\delta\omega \quad (2.5)$$

$$\delta\omega = cos(\alpha)\delta\alpha\delta\varphi \quad (2.6)$$

$$cos(\sigma) = cos(\beta)sin(\alpha) + sin(\beta)cos(\alpha)cos(\varphi) \quad (2.7)$$

where $R_{\alpha\varphi}$ is the radiance of an unobstructed sky element at altitude α and azimuth φ in the sky dome (W/m²·sr), ω is the solid angle (sr), σ is the angle between the sky element at (α, φ) and the normal of the surface (degree). The

detail of sky angle is shown in Figure 1. To this, the $I_{\beta D}$ can be determined by double integrating by Equation (2.8) as follows (Li et al., 2016):

$$I_{\beta D} = \int_{\varphi_1}^{\varphi_2}\int_{\alpha_1}^{\alpha_2} R_{\alpha\varphi}\left[cos(\beta)sin(\alpha)+sin(\beta)cos(\alpha)cos(\varphi)\right]cos(\alpha)\delta\alpha\delta\varphi \tag{2.8}$$

The ranges for α and φ are from 0 to $\pi/2$ and from 0 to 2π, respectively. To consider the sky element in unobstructed and obstructed parts. The double integrating by Equation (2.9) can be expressed as:

$$\begin{aligned} I_{\beta D} &= cos\beta\left[\sum_i^n R_{\alpha\varphi i}\left(\int_{\varphi_{iL}}^{\varphi_{iL}+\delta_{\varphi i}}\delta\phi\right)\left(\int_{\max(\alpha_{iL},\alpha p)}^{\max(\alpha_{iL+\delta\alpha_i},\alpha p)} sin\beta cos\alpha\delta\alpha\right)\right] \\ &\quad + sin\beta\left[\sum_i^n R_{\alpha\varphi i}\left(\int_{\varphi_{iL}}^{\varphi_{iL}+\delta_{\varphi i}} cos\varphi\delta\varphi\right)\left(\int_{\max(\alpha_{iL},\alpha p)}^{\max(\alpha_{iL+\delta\alpha_i},\alpha p)} cos^2\alpha\delta\alpha\right)\right] \end{aligned} \tag{2.9}$$

where $R_{\alpha\varphi i}$ is the radiance of the ith sky element, which varies between different sky elements. The angles α_{iL} and φ_{iL} represent the lower limits of the altitude and azimuth angles for the ith sky element (degree), corresponding to the increments $\delta\alpha_i$ and $\delta\varphi_i$, respectively.

The angle αp represents the threshold below which the sky element is unobstructed from an inclined plane. These angles are illustrated in Figure 1(a) and 1(b). The details of this method can be found in (Li and Lam, 2007) and (Li et al., 2016).

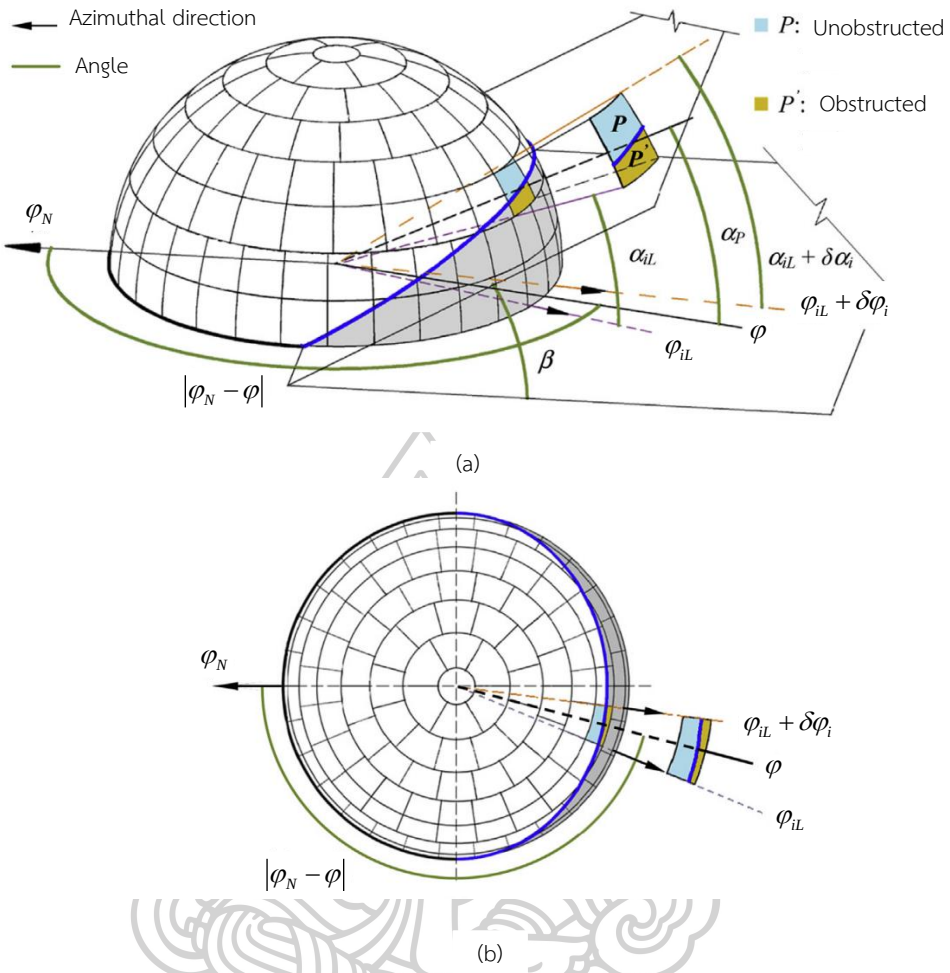

Figure 1 Angles defining the position of a sky point in unobstructed and obstructed inside view (a) and top view (b).

2.5 Sky radiance measurement

The most accurate measurement of sky radiance at the Earth's surface is achieved using sky scanners. Specific models, such as the MS-321LR sky scanner manufactured by EKO in Japan, employ a silicon photodiode sensor to measure radiance and luminance (Ineichen and Molineaux, 1993), as illustrated in Figure 2. To ensure precise sky luminance measurements, the silicon photodiode is typically combined with optical filters designed to match the standard photopic response curve. This configuration guarantees that luminance measurements accurately correspond to human visual perception.

The EKO sky scanner is equipped with two sensors, enabling the measurement of sky radiance within a range of 0–300 W/m²·sr and sky luminance within a range of 0–50 kcd/m². An example of sky luminance and sky radiance data obtained from EKO sky scanner at Nakhon Pathom station, Thailand is shown in Figure 3. These measurements are taken at 145 predefined points across the sky dome, following the distribution proposed by Tregenza (Tregenza, 1987). The sensors are mounted on two-step motors that facilitate precise rotation to specified altitude and azimuth angles, ensuring comprehensive sky coverage. A silicon photodiode sensor operates as a semiconductor device that converts incident light into a voltage through the photoelectric effect. This voltage is subsequently converted into radiometric and photometric units (W/m²·sr and kcd/m²) by dividing it by the sensitivity factor provided by the manufacturer.

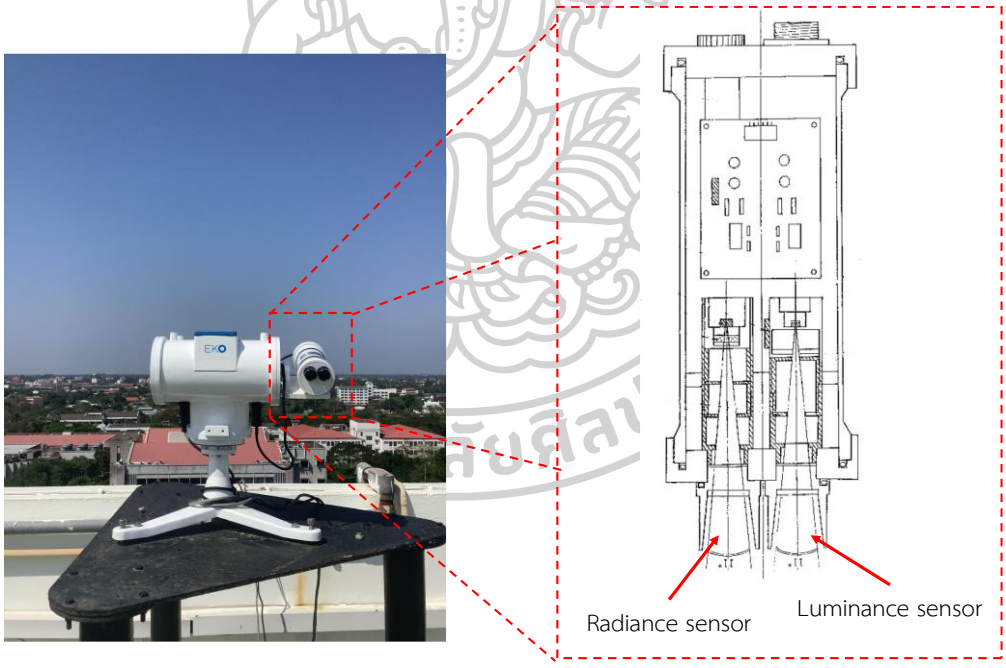

Figure 2 Image of the EKO sky scanner captured at Nakhon Pathom station (front view) (a) and a schematic diagram of the head sensor (top view) (b).

Although sky radiance can be measured using a sky scanner, its high cost, frequent instability, and maintenance requirements have led to a lack of sky radiance measurements in many locations. Consequently, a mathematical model for calculating sky radiance data based on sky conditions is the next best alternative to sky scanners in terms of accuracy (CIE, 2003).

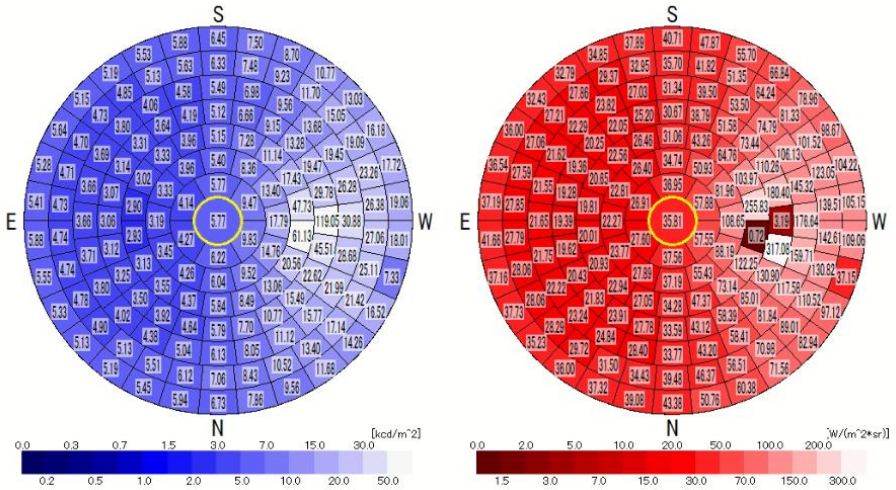

(Sky luminance) (Sky radiance)

Figure 3 An example of sky luminance and sky radiance data from the EKO sky scanner (Model: MS-321LR).

2.6 Literature review

Many models have been developed to calculate R / R_z. This study reviews and summarizes the historical development of R / R_z modeling as follows:

It is very important to remember that R / R_z is related to L / L_z because both originate from the sun and can be calculated using the same equation. Therefore, the literature review on R / R_z will begin with L / L_z models due to their early development and long history. L / L_z on a partly cloudy day is highly random and complex due to varying cloud conditions. As a result, most early studies of L / L_z focused on clear and overcast sky conditions, as these types present well-defined, single conditions that are easier to model. The first empirical formula to describe overcast skies was the Moon and Spencer model (Moon and Spencer, 1942), which

was later adopted by the CIE in 1955 as the CIE standard overcast sky. This was followed by the Kittler model (Kittler, 1967), which proposed a L/L_z model specifically for clear skies and was formally recognized by the CIE in 1973 as the CIE standard clear sky. However, models for clear and overcast skies are not generally applicable to all sky conditions. In 1993, the Perez all-weather sky model (Perez et al., 1993) categorized L/L_z into eight types, covering a broad range of conditions from overcast to clear skies. This model significantly advanced the understanding of L/L_z variations under real-world atmospheric conditions

In 1980, Hooper and Brunger (Brunger and Hooper, 1993) identified limitations in the L/L_z model, which calculates R/R_z. They found that this approach introduces uncertainties in energy applications. To address this issue, they developed the first direct model for calculating R/R_z. Their model improves accuracy by summing the contributions of three key components: the isotropic component, the circumsolar region, and the horizontal brightness. The Hooper and Brunger model represented by the following expression:

$$\frac{R}{R_z} = I_{dh}\left[\frac{a_0 + a_1 sin(\alpha) + a_2 exp(-a_3\chi)}{\pi(a_0 + 2a_1/3) + 2a_2 I(\mathrm{Z}, a_3)}\right] \tag{2.10}$$

$$I(\mathrm{Z}, a_3) = I_1\left[\pi - I_4(1 - I_2/I_3)\right] \tag{2.11}$$

$$I_1 = \left[1 + exp(-a_3\pi/2)/a_3^{\,2} + 4\right] \tag{2.12}$$

$$I_2 = 2\left[1 - exp(-a_3\pi)\right] \tag{2.13}$$

$$I_3 = a_3\pi\left[1 + exp(-a_3\pi/2)\right] \tag{2.14}$$

$$I_4 = 2Z_s sin(Z_s) sin(2Z_s) \tag{2.15}$$

The coefficient a_0, a_1, a_2, a_3 are depends on diffuse fraction (K_d) and clearness index (K_t) as demonstrated in Table 1-4.

Table 1 Coefficient a_0 of Hooper and Brunger model.

K_d \ K_t	0.05	0.15	0.25	0.35	0.45	0.55	0.65	0.75	0.85
0.95	0.1864	0.2002	0.138	0.1508	0.1718	0.206	0.1605	0.1482	0.1505
0.85	0.1431	0.2303	0.3477	0.2664	0.2139	0.152	0.1151	0.1358	0.1529
0.75	0.2213	0.2995	0.3687	0.2684	0.201	0.187	0.1842	0.1566	0.17
0.65	0.2818	0.3423	0.3851	0.2843	0.2713	0.1597	0.2088	0.1273	0.1834
0.55	0.3784	0.4751	0.6079	0.2892	0.2816	0.2465	0.207	0.2477	0.2396
0.45	0.4132	0.4479	0.4208	0.2337	0.2822	0.2916	0.2583	0.2457	0.2315
0.35	0.4055	0.3979	0.3478	0.2749	0.3162	0.3006	0.2871	0.2491	0.251
0.25	0.3834	0.3614	0.3249	0.3019	0.3289	0.3417	0.3153	0.3071	0.2971
0.15	0.3624	0.3414	0.3214	0.3179	0.3339	0.3388	0.336	0.3243	0.3061

Table 2 Coefficient a_1 of Hooper and Brunger model.

K_d \ K_t	0.05	0.15	0.25	0.35	0.45	0.55	0.65	0.75	0.85
0.95	0.1979	0.1772	0.093	0.5472	0.0566	-0.029	0.0755	0.1579	0.1649
0.85	0.142	0.0346	-0.215	-0.159	0.307	0.1497	0.1805	0.2404	0.1719
0.75	0.0064	-0.129	-0.292	-0.161	-0.127	-0.063	0.0253	0.3003	0.1034
0.65	-0.097	-0.2	-0.272	-0.164	-0.183	-0.171	-0.052	-0.05	-0.093
0.55	-0.219	-0.342	-0.483	-0.195	-0.194	-0.124	-0.092	-0.071	-0.136
0.45	-0.268	-0.317	-0.292	-0.101	-0.184	-0.206	-0.165	-0.139	-0.202
0.35	-0.269	-0.27	-0.222	-0.152	-0.203	-0.217	-0.218	-0.222	-0.09
0.25	-0.253	-0.238	-0.207	-0.191	-0.23	-0.257	-0.233	-0.257	-0.312
0.15	-0.239	-0.225	-0.212	-0.218	-0.244	-0.258	-0.26	-0.3	-0.453

Table 3 Coefficient a_2 of Hooper and Brunger model.

K_d \ K_t	0.05	0.15	0.25	0.35	0.45	0.55	0.65	0.75	0.85
0.95	0	0	0.289	0.665	0.873	2.951	2.589	2.314	2.096
0.85	2.636	2.651	5.317	1.775	1.609	1.831	2.228	2.035	1.878
0.75	2.637	2.638	2.626	4.522	1.409	1.281	1.308	1.848	1.717
0.65	3.027	3.417	4.196	5.296	2.822	1.296	1.322	1.596	1.589
0.55	5.137	7.247	11.07	2.134	3.86	2.916	1.109	1.583	1.581
0.45	7.239	9.341	11.43	11.79	6.03	2.732	1.952	1.512	1.58
0.35	8.51	9.781	10.22	9.007	6.222	4.544	2.646	1.599	0.973
0.25	8.866	9.222	8.664	7.107	5.207	4.191	3.886	2.312	1.359
0.15	8.56	8.255	7.287	5.91	4.713	4.129	4.248	1.915	1.612

Table 4 Coefficient a_3 of Hooper and Brunger model.

K_d \ K_t	0.05	0.15	0.25	0.35	0.45	0.55	0.65	0.75	0.85
0.95	1	1	0.9667	1.675	2.41	3.722	3.938	6.6941	7.864
0.85	5.525	3.648	4.421	2.859	3.726	4.612	4.155	9.449	9.034
0.75	4.385	3.245	2.841	4.084	2.245	2.593	3.112	14.74	8.618
0.65	4.318	4.252	5.259	4.367	3.486	1.918	2.836	2.099	2.492
0.55	4.369	4.42	4.588	3.726	3.744	4.076	2.558	3.45	2.886
0.45	4.534	4.699	4.978	5.369	4.524	3.762	3.376	2.964	2.322
0.35	4.768	5.002	5.306	5.633	5.897	4.266	3.594	2.64	2.677
0.25	4.969	5.171	5.339	5.372	5.112	4.326	4.392	3.518	2.397
0.15	5.076	5.183	5.195	5.051	4.73	4.349	4.372	3.268	2.319

Afterward, in 1997, Kittler, Darula, and Perez worked together to improve the classification of L / L_z, leading to the creation of 15 sky types. These types are defined by five key coefficients that describe how daylight is distributed across the sky. The classification covers a wide range of sky conditions, from fully overcast to completely clear skies. In 2003, the CIE (CIE, 2003) officially adopted the 15 standard sky types (known as the 15 CIE standard general sky) and subsequently approved by the International Organization for Standardization (ISO) in 2004.

According to the CIE model, L / L_z is commonly described in terms of relative value, as it is difficult to directly quantify L (Igawa et al., 2004), it is given by:

$$\frac{L}{L_z} = \frac{f(\chi)\varphi(Z)}{f(Z_s)\varphi(0^\circ)} \tag{2.16}$$

$$\frac{\varphi(Z)}{\varphi(0^\circ)} = \frac{1+aexp(b/cos(Z))}{1+aexp(b)} \tag{2.17}$$

$$\frac{f(\chi)}{f(Z_s)} = \frac{1+c\left[exp(d\chi)-exp(d\pi/2)\right]+ecos^2(\chi)}{1+c\left[exp(dZ_s)-exp(d\pi/2)\right]+ecos^2(Z_s)} \tag{2.18}$$

where Z is the zenith angle of the sky point (rad), Z_s is the solar zenith angle (rad), χ is the angular distance between the sun and the sky point (rad) that is given by cosine law as follows:

$$\chi = arccos\left(cos(Z_s)cos(Z)+sin(Z_s)sin(Z)cos(|\phi-\phi_s|)\right) \tag{2.19}$$

To apply the CIE model using L / L_z, it is necessary to account for solar positions, sky conditions, and turbidity levels to select the appropriate model coefficients, as shown in Table 5.

Table 5 Sky description according to 15 CIE standard skies.

No.	Coefficients of Equation (2.16)					Sky description
	a	*b*	*c*	*d*	*e*	
1	4	-0.7	0	-1	0	CIE standard overcast sky, steep luminance gradation towards zenith, azimuthal uniformity
2	4	-0.7	2	-1.5	0.15	Overcast, with steep luminance gradation and slight brightening towards the sun
3	1.1	-0.8	0	-1	0	Overcast, moderately graded with azimuthal uniformity
4	1.1	-0.8	2	-1.5	0.15	Overcast, moderately graded and slight brightening towards the sun
5	0	-1	0	-1	0	Sky of uniform luminance
6	0	-1	2	-1.5	0.15	Partly cloudy sky, no gradation towards zenith, slight brightening towards the sun
7	0	-1	5	-2.5	0.3	Partly cloudy sky, no gradation towards zenith, brighter circumsolar region
8	0	-1	10	-3	0.45	Partly cloudy sky, no gradation towards zenith, distinct solar corona
9	-1	-0.55	2	-1.5	0.15	Partly cloudy, with the obscured sun
10	-1	-0.55	2	-2.5	0.3	Partly cloudy, with brighter circumsolar region
11	-1	-0.55	10	-3	0.45	White-blue sky with distinct solar corona
12	-1	-0.32	10	-3	0.45	CIE standard clear sky, low luminance turbidity
13	-1	-0.32	16	-3	0.3	CIE standard clear sky, polluted atmosphere
14	-1	-0.15	16	-3	0.3	Cloudless turbid sky with broad solar corona
15	-1	-0.15	24	-2.8	0.15	White-blue turbid sky with broad solar corona

The process of categorizing sky types is complex and often depends on the personal skill and experience of the observer. Variations in atmospheric conditions and cloud coverage can make classification subjective, which can influence the

accuracy of L/L_z models. As a result, the expertise required for precise sky type classification plays a crucial role in the reliability of daylight simulations and environmental analysis. Over the past decade, a variety of methods have been developed and applied in different countries to classify sky conditions based on meteorological data.

In 2004, Igawa et al. (Igawa et al., 2004) developed a model to calculate R/R_z using the sky index (S_i). The Igawa model uses the same equation as the CIE model, but it is more general than the CIE model because its coefficient better represents different sky conditions by using meteorological measurement data, which are given by:

$$a = \frac{4.5}{1+0.15exp(3.4S_i)} - 1.04 \quad (2.20)$$

$$b = \frac{-1}{1+0.17exp(1.3S_i)} - 0.05 \quad (2.21)$$

$$c = 1.77(1.22S_i)^{3.56} exp(0.2S_i)(2.1-S_i)^{0.8} \quad (2.22)$$

$$d = \frac{-3.05}{1+10.6exp(-3.4S_i)} \quad (2.23)$$

$$e = \frac{0.48}{1+245exp(-4.13S_i)} \quad (2.24)$$

The S_i is calculated using two indices: the clear sky index (K_c) and the cloudless index (CL). The clear sky index is based on global solar irradiance, while the cloudless index is based on both global solar irradiance and diffuse solar irradiance. The S_i is given by:

$$S_i = K_c + CL^{0.5} \quad (2.25)$$

$$K_c = \frac{I_{HG}}{0.84(I_0 / m)exp(-0.0675m)} \quad (2.26)$$

$$CL = \frac{1-Ce}{1-Ce_s} \quad (2.27)$$

$$Ce = \frac{I_{HD}}{I_{HG}} \quad (2.28)$$

$$Ce_s = 0.01299 + 0.07698m - 0.003857m^2 + 0.0001054m^3 - 0.000001031m^4 \quad (2.29)$$

where m is air mass (-).

In 2021, García-Rodríguez et al. (García-Rodríguez et al., 2020) demonstrated the image of each sky type, as shown in Figure 4.

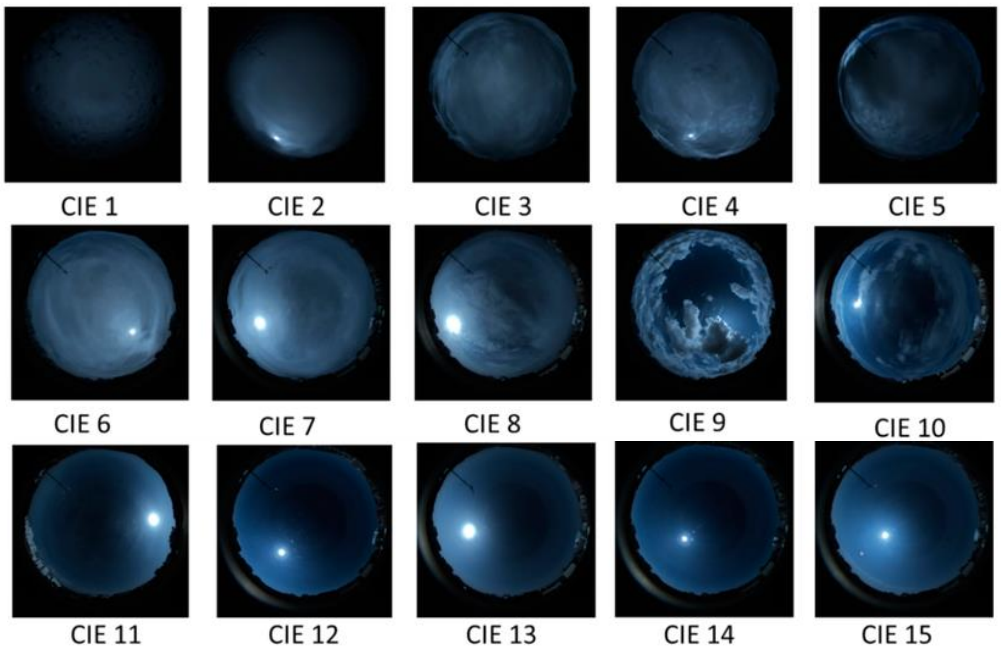

Figure 4 Images representing the 15 CIE standard sky types.

In 2024, Yao et al. (Yao et al., 2024) further refined R/R_z modeling by classifying sky conditions into 15 different types based on the CIE standard sky model, using the clearness index (K_t). This study investigated the relationship between R/R_z and L/L_z within each category, resulting in an enhanced CIE model for calculating R/R_z.

$$f\left(\frac{R}{R_z}\right)^3 + g\left(\frac{R}{R_z}\right)^2 + h\left(\frac{R}{R_z}\right) + i = \frac{L}{L_z} \tag{2.30}$$

The coefficient for the R/R_z, based on the K_t, is shown in Table 6.

Table 6 Coefficients of R/R_z are based on Equation 2.30.

No.	Coefficients of Equation (2.30)								
	a	b	c	d	e	f	g	h	i
1	4	-0.7	0	-1	0	0.000055	-0.01151	0.603667	0.3284
2	4	-0.7	2	-1.5	0.15	0.000771	-0.03902	0.713694	0.213714
3	1.1	-0.8	0	-1	0	0.000561	-0.03821	0.625276	0.263439
4	1.1	-0.8	2	-1.5	0.15	0.009157	-0.19714	1.095097	0.024975
5	0	-1	0	-1	0	-0.14447	0.420705	0.247501	0.323612
6	0	-1	2	-1.5	0.15	0.000153	-0.02083	0.772748	0.186576
7	0	-1	5	-2.5	0.3	0.002185	-0.04339	0.877156	0.122464
8	0	-1	10	-3	0.45	0.000047	-0.01547	0.842815	0.13138
9	-1	-0.55	2	-1.5	0.15	0.15	0.000165	-0.02372	0.911789
10	-1	-0.55	2	-2.5	0.3	0.000039	-0.01218	0.832418	0.206391
11	-1	-0.55	10	-3	0.45	0	0.154544	0.793559	0.099388
12	-1	-0.32	10	-3	0.45	-0.09981	0.665642	0.454672	0.132873
13	-1	-0.32	16	-3	0.3	0.000023	-0.00653	0.777474	0.278132
14	-1	-0.15	16	-3	0.3	-0.00004	-0.00227	0.682462	0.389883
15	-1	-0.15	24	-2.8	0.15	-0.00005	-0.01473	0.927674	0.040821

In the case of Thailand, in 2007, Chaiwiwatworakul and Chirarattananon (Chirarattananon and Chaiwiwatworakul, 2007) adjusted the coefficients for L/L_z (a to e) and R/R_z (a_r to e_r) model according to Equation (2.16) to suit tropical climate conditions, using annual sky scanner data measured from January 1999 to December 2002 in Bangkok (14.08°N, 100.62°E), as presented in Table 7.

Table 7 Adjusted values of parameters for L/L_z and R/R_z models for tropical climate according to Equation (2.16).

No.	Coefficients of L/L_z					Coefficients of R/R_z				
	a	b	c	d	e	a_r	b_r	c_r	d_r	e_r
1	4.15	-0.7	0	-1.3	0.06	4.25	-0.7	0	-1.3	0.07
2	2	-0.7	1.4	-1.31	0.1	2	-0.7	1.4	-1.31	0.10
3	1.15	-0.8	0	-1.01	0.05	1.25	-0.89	0.1	-1.01	0.05
4	0.5	-0.8	2	-1.34	0.1	0.6	-0.7	2	-1.35	0.12
5	-0.35	-1.08	0	-1.3	0.09	-0.45	-1.35	0	-1.3	0.08
6	-0.35	-1.35	2.5	-1.53	0.17	-0.45	-1.35	2.5	-1.49	0.17
7	-0.45	-1.35	5.3	-2.24	0.2	-0.45	-1.35	5.3	-2.22	0.20
8	-0.95	-1.26	9.1	-2.7	0.35	-0.8	-1.12	9.2	-2.7	0.35
9	-1	-0.66	2.5	-1.39	0.2	-1	-0.72	2.5	-1.38	0.20
10	-1	-0.66	5.7	-2.44	0.26	-1	-0.73	6	-2.43	0.25
11	-1	-0.6	10.4	-2.7	0.35	-1	-0.67	10.7	-2.7	0.35
12	-1	-0.3	10.7	-2.99	0.35	-1	-0.32	11.1	-3	0.35
13	-1	-0.3	14.7	-2.97	0.27	-1	-0.4	14.8	-2.94	0.27
14	-1	-0.13	14.4	-3	0.2	-1	-0.22	14.6	-3	0.20
15	-1	-0.13	20	-2.9	0.15	-1	-0.24	20	-2.9	0.15

In 2017, Tohsing et al. (Tohsing et al., 2017) characterized three years of R measurements obtained using an EKO sky scanner at a tropical station in Nakhon

Pathom (13.82°N, 100.04°E), Thailand as shown in Figure 5, for local times 9:30 4(a), 12:30 4(b), and 15:30 4(c). The black dot denotes the sun's position and its surrounding circumsolar region.

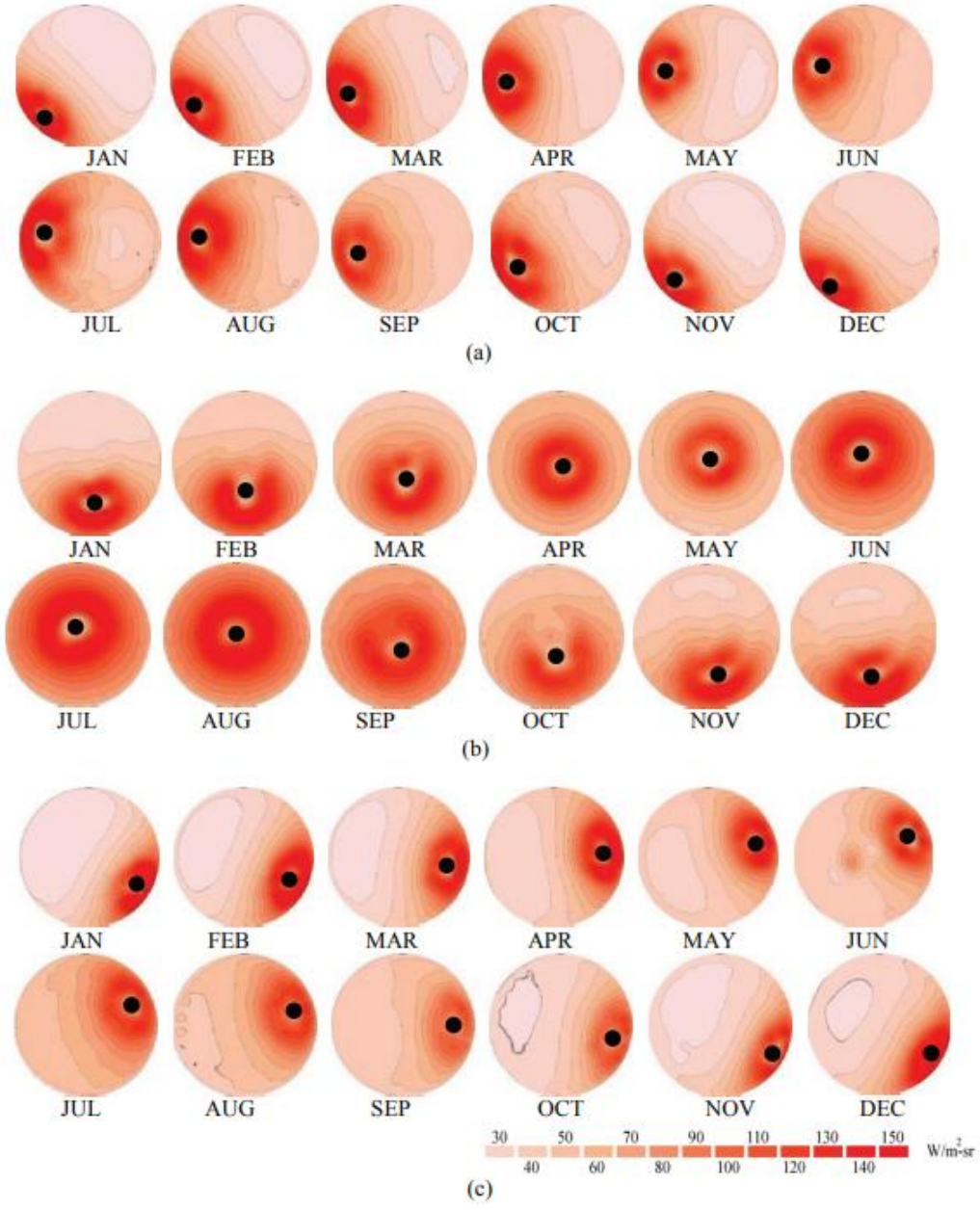

Figure 5 Monthly averaged clear sky R / R_z over a three-year period (2013–2015) for Thailand at 9:30 4(a), 12:30 4(b), and 15:30 4(c) at local time.

As highlighted in the literature, the CIE standard sky model was initially developed for L / L_z estimation, applying it directly to predict solar radiation on PV modules can introduce uncertainties in power output estimations. Moreover, ground-based observations and human classification methods based on the CIE model are often subjective and depend on individual interpretation, which may further reduce the reliability of sky condition assessments for PV applications. To address this limitation, the present study focuses on estimating sky radiance in both R / R_z and R_z, as detailed in the following chapter.

Chapter 3

A model for calculating relative sky radiance under all sky conditions using geostationary satellite data*

3.1 Introduction

Applying the CIE standard sky model involves considering several factors, including the sun's position, sky conditions, and atmospheric turbidity, to select appropriate model coefficients. This process can be complex and depends heavily on observer conditions. In the last decade, a variety of CIE standard sky models have been applied to calculate L/L_z and R/R_z over different locations. It is important to note that the CIE standard sky model was initially developed to calculate L/L_z, primarily for optimizing energy efficiency in building lighting. Although early studies have applied the CIE standard sky model to calculate R/R_z (Li et al., 2016; Lou et al., 2016), in some conditions, the effects of atmospheric and meteorological factors can lead to significant differences in both L/L_z and R/R_z (Gueymard and Kocifaj, 2022).

Geostationary weather satellite data have become increasingly popular for deriving cloud information due to their high spatial and temporal resolution (Cano et al., 1986; Hammer et al., 2003; Janjai et al., 2003). Therefore, in this study, we developed a simplified mathematical formula to obtain R/R_z under all sky conditions in a tropical environment using the cloud index (n) derived from geostationary satellite data to address the lack of spatial sky radiance data.

3.2 Materials and methods

3.2.1 Measurement sites

To represent the diverse geographical and climatic characteristics of each region in Thailand, the following observation stations were selected: Chiang Mai in northern Thailand (18.78°N, 98.98°E; 313 m above sea level), Nakhon Pathom in

* This paper has been published to Renewable Energy (Q1).

central Thailand (13.82°N, 100.04°E; 10 m above sea level), Ubon Ratchathani in northeastern Thailand (15.25°N, 104.04°E; 127 m above sea level), and Songkhla in southern Thailand (7.20°N, 100.60°E; 5 m above sea level). The distribution of these stations are shown in Figure 5.

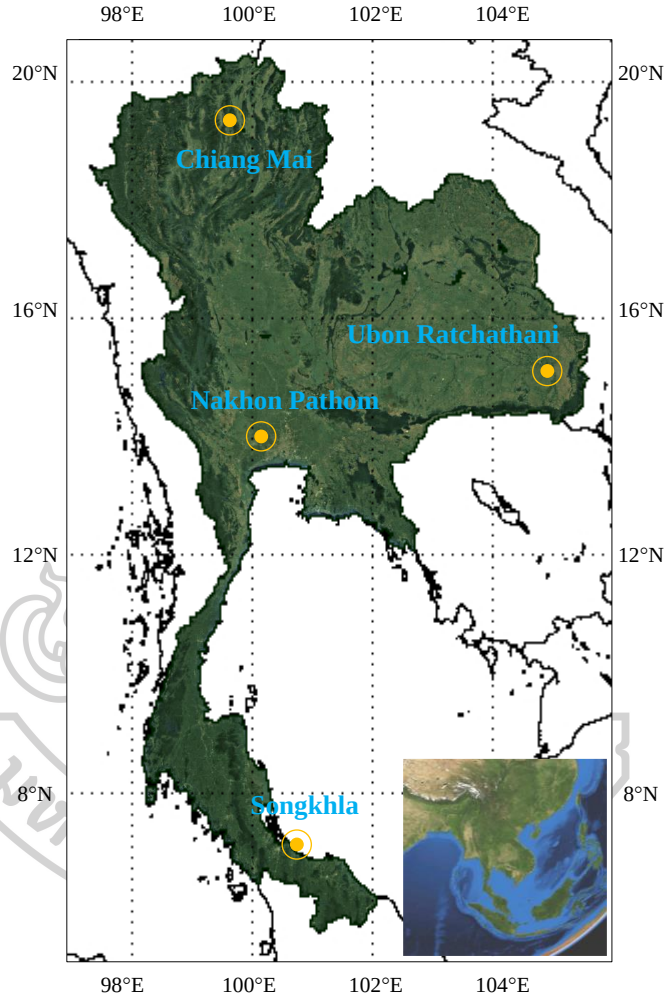

Figure 6 Geographical characteristics and distribution of the selected locations in Thailand.

3.2.2 Data and quality control

The data used to develop a model for calculating R/R_z in this study includes both ground measurement data and satellite observation data which the details are described as follows.

3.2.2.1 Ground measurement data

The ground measurement data used in this study comprised sky radiance, global and diffuse solar irradiance. Sky radiance data collected at Nakhon Pathom station between January 2013 and December 2017 were used to develop the relative sky radiance model. To ensure the accuracy of the model for a tropical environment, the sky radiance data at Chiang Mai station from January to December 2016, Ubon Ratchathani station from January to December 2011, and Songkhla station from January to December 2008 were used for model validation. Continuous long-term data measurement poses significant challenges due to issues such as prolonged instrument usage and costs, which can lead to data acquisition interruptions. The historical data used in this study spans over five years, while current climate conditions show significant variability and divergence from past patterns. To account for the present climate conditions, sky radiance data were collected at Nakhon Pathom station from November 2023 to October 2024 and were used to compare the proposed model against other existing sky models. The sky radiance data collected from 8:30 to 16:30 at local time correspond to satellite data.

For comparison with existing models, CMP21 and CMP11 pyranometers (Kipp and Zonen) were installed at the Nakhon Pathom station in 2024 to measure global and diffuse solar irradiance, respectively. A CMP11 pyranometer equipped with a 2AP sun tracker (Kipp and Zonen) and a shadow ball was used to measure diffuse solar irradiance.

To eliminate erroneous data caused by equipment malfunctions, power failures, and other issues, compromised EKO sky scanner and solar irradiance measurement data were excluded from the dataset and omitted from the analysis, following the methodologies outlined by Li and Cheung (Li and Cheung, 2005) and Lou et al. (Lou et al., 2016).

Furthermore, to verify the sky conditions obtained from satellite images, cloud cover data were retrieved from two sky cameras: PREDE sky camera (PSV-100) that captured images from January 2013 to December 2017, and EKO sky camera (ASI-16) that captured images from November 2023 to October 2024. These sky cameras are

digital cameras with a fisheye lens, providing a 180° field of view to record images of the sky dome installed at the ground surface.

3.2.2.2 Satellite observation data

Most satellites that serve as a good source of weather information are geostationary satellites due to their high spatial and temporal resolution. Over the past decade, numerous studies have employed satellite images to gather cloud information, often represented as a n. In this study, n data from the Himawari satellite series, operated by the Japan Meteorological Agency (JMA), were employed. This includes data from MTSAT-1R in 2008, MTSAT-2 covering January 2013 to December 2015, Himawari-8 from January 2016 to December 2017, and Himawari-9 from November 2023 to October 2024. These satellites capture images in the visible wavelengths, covering the Asia-Pacific region with a spatial resolution of 3 × 3 km. Each pixel in these images contains a gray level value that can be converted to pseudo-reflectivity using a calibration table provided by the satellite agency, with values ranging from 0 to 1. Then, the pseudo-reflectivity was divided by the cosine of the local solar zenith angle to provide the earth-atmosphere reflectivity (ρ_{EA}). In the final step, the ρ_{EA} was subsequently used to derive the n given by Cano et al. (Cano et al., 1986). The Cano method is a widely used semi-empirical approach for calculating n. Its implementation remains largely unaffected by variations in satellite platforms, as the n derived from this method normalizes observed reflectance between clear (ground reflectivity or ρ_G) and overcast (cloud reflectivity or ρ_C) sky conditions, as described in Equation (3.1). This method has been globally applied using various geostationary satellites, including GMS, MTSAT-2, GOES, and Himawari-8. The n based on the Cano method is represented as follows:

$$n = \frac{\rho_{EA} - \rho_G}{\rho_C - \rho_G} \tag{3.1}$$

To obtain the ρ_G, the minimum value of the ρ_{EA} or cloud-free pixels was composited. The ρ_G can change due to variations in soil moisture and plant growth.

Therefore, the monthly average hourly ρ_{EA} were composited to derive a constant monthly ρ_G. The values of ρ_C was estimated from the maximum value of the ρ_{EA}. Further details on the calculation of the n can be found in some of our previous studies Janjai et al. (Janjai et al., 2003).

Consider for example, from Equation (3.1), when the given pixel or the ρ_{EA} is covered by a cloud, n value will equal 1. Thus, n values range from 0 (indicating clear sky conditions) to 1 (indicating overcast sky conditions). This demonstrates that n can effectively represent the amount of cloud cover. In this study, the values of n were averaged over a 9 × 9 pixels surrounding the stations of interest to derive the n, which was used for classifying sky conditions. The satellite images taken every half hour from 8:30 to 16:30 local time were selected.

3.2.3 Description of the methodology

This section describes the details of the CIE standard sky model and the proposed model for calculating R/R_z, which are presented as follows:

3.2.3.1 Proposed model

The main objective of this study aimed to simplify an empirical model by using satellite data in terms of n to classify sky conditions for calculating R/R_z under all sky conditions. The steps are outlined below.

1) Data preparation

- Before averaging the data, it is important to note that the appearance of the sun over the sky dome changes over time. Therefore, it is necessary to rotate the sun's position in each sky dome to the reference direction to ensure that each set of sky radiance data is comparable in terms of zenith and azimuth angles. In this study, the south direction is considered as the reference.
- Each set of sky radiance was then classified into 10 groups according to sky conditions: $0 < n \leq 0.1$, $0.1 < n \leq 0.2$, $0.2 < n \leq 0.3$, $0.3 < n \leq 0.4$,

$0.4 < n \leq 0.5$, $0.5 < n \leq 0.6$, $0.6 < n \leq 0.7$, $0.7 < n \leq 0.8$, $0.8 < n \leq 0.9$ and $0.9 < n \leq 1.0$.

- Then, the sets of sky radiance for each sky condition were sorted into 8 groups based on Z_s: $0° < Z_s \leq 10°$, $10° < Z_s \leq 20°$, $20° < Z_s \leq 30°$, $30° < Z_s \leq 40°$, $40° < Z_s \leq 50°$, $50° < Z_s \leq 60°$, $60° < Z_s \leq 70°$ and $70° < Z_s \leq 80°$.

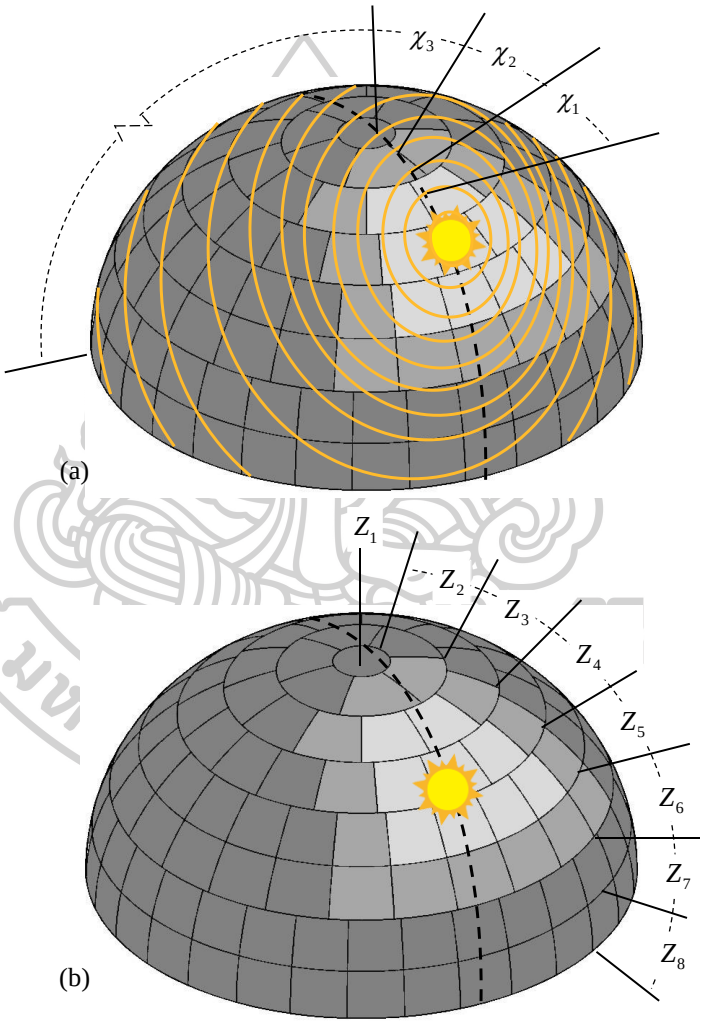

Figure 7 Graphic of the sky dome showing the gradient zones around the sun (a) and zenith zones (b).

- From the grouping, a total of 80 (10 groups of n × 8 groups of Z_s) subgroups of sky radiance according to Z_s and sky conditions were obtained. The sky radiance in each 80 subgroup was then averaged to represent the sky radiance in each sky dome or 145 points in each subgroup.
- The averaged sky radiance data in each of the 80 subgroups were grouped into 30 zones based on the indicatrix zones around the sun or χ angle (as shown in Figure 6(a)) at 6° < χ_1 ≤ 10°, 10° < χ_2 ≤ 15°, 15° < χ_3 ≤ 20°, 20° < χ_4 ≤ 25°, 25° < χ_5 ≤ 30°, 30° < χ_6 ≤ 35°, 35° < χ_7 ≤ 40°, 40° < χ_8 ≤ 45°, 45° < χ_9 ≤ 50°, 50° < χ_{10} ≤ 55°, 55° < χ_{11} ≤ 60°, 60° < χ_{12} ≤ 65°, 65° < χ_{13} ≤ 70°, 70° < χ_{14} ≤ 75°, 75° < χ_{15} ≤ 80°, 80° < χ_{16} ≤ 85°, 85° < χ_{17} ≤ 90°, 90° < χ_{18} ≤ 95°, 95° < χ_{19} ≤ 100°, 100° < χ_{20} ≤ 105°, 105° < χ_{21} ≤ 110°, 110° < χ_{22} ≤ 115°, 115° < χ_{23} ≤ 120°, 120° < χ_{24} ≤ 125°, 125° < χ_{25} ≤ 130°, 130° < χ_{26} ≤ 135°, 135° < χ_{27} ≤ 140°, 140° < χ_{28} ≤ 145°, 145° < χ_{29} ≤ 150°, and 150° < χ_{30} ≤ 155°. To prevent damage to the sensor from high radiance values (typically exceeding 300 W/m²·sr near the circumsolar region). The EKO sky scanner automatically activates its shelter, resulting in sky radiance data values close to zero or negative. Then, the χ angle were start with 6° following the methodology outlined by (Lou et al., 2022).
- The averaged sky radiance data were also grouped into 8 gradient zones corresponding to the Z of a EKO sky scanner at Z_1 = 0°, Z_2 = 12°, Z_3 = 24°, Z_4 = 36°, Z_5 = 48°, Z_6 = 60°, Z_7 = 72° and Z_8 = 84° as also shown in Figure 6(b).

For the proposed model, we divided the CIE standard sky model into two terms: the $\varphi(Z)/\varphi(0^\circ)$ and $f(\chi)/f(Z_s)$ functions. Since the mathematical expressions of these two functions are complex and involve multiple variables, separating them presents a significant challenge. However, the zoning and intersection methods presented in this study enabled the separation of the $\varphi(Z)/\varphi(0^\circ)$ function from the $f(\chi)/f(Z_s)$ function and vice versa.

2) Eliminating the $f(\chi)/f(Z_s)$ function

To eliminating the $f(\chi)/f(Z_s)$ function from the $\varphi(Z)/\varphi(0^\circ)$ function. Firstly, considering a given χ zone, the variation of χ zone is constant at different Z zone. Secondly, determined the sky radiance that intersection between each Z zone and χ zone. For example, at χ_1, the formula of R/R_z from Equation (1.16) can be reformulated and transferred into the form shown in Equation (3.2) to Equation (3.4):

$\chi_1,\ Z_1;$ $$\frac{R(Z_1,\chi_1)}{R_z} = \frac{\varphi(Z_1)}{\varphi(0^\circ)} \cdot \frac{f(\chi_1)}{f(Z_s)} \quad (3.2)$$

$\chi_1,\ Z_2;$ $$\frac{R(Z_2,\chi_1)}{R_z} = \frac{\varphi(Z_2)}{\varphi(0^\circ)} \cdot \frac{f(\chi_1)}{f(Z_s)} \quad (3.3)$$

$$\vdots$$

$\chi_1,\ Z_8;$ $$\frac{R(Z_8,\chi_1)}{R_z} = \frac{\varphi(Z_8)}{\varphi(0^\circ)} \cdot \frac{f(\chi_1)}{f(Z_s)} \quad (3.4)$$

The $f(\chi_1)/f(Z_s)$ function on the right-hand side remains the same from Equation (3.2) to Equation (3.4). By selecting the reference formula at a given χ zone, the $f(\chi)/f(Z_s)$ function can be canceled out by dividing the reference formula. In this present, we choose the Z = 48° or Z_5 as the reference formula ($Z_5 = Z_{ref}$), expressed as:

$\chi_1,\ Z_1;$ $$\frac{\frac{R(Z_1,\chi_1)}{R_z}}{\frac{R(Z_{ref},\chi_1)}{R_z}} = \frac{\frac{\varphi(Z_1)}{\varphi(0^\circ)} \cdot \frac{f(\chi_1)}{f(Z_s)}}{\frac{\varphi(Z_{ref})}{\varphi(0^\circ)} \cdot \frac{f(\chi_1)}{f(Z_s)}} \quad (3.5)$$

$\chi_1,\ Z_2;$ $$\frac{\frac{R(Z_2,\chi_1)}{R_z}}{\frac{R(Z_{ref},\chi_1)}{R_z}} = \frac{\frac{\varphi(Z_2)}{\varphi(0^\circ)} \cdot \frac{f(\chi_1)}{f(Z_s)}}{\frac{\varphi(Z_{ref})}{\varphi(0^\circ)} \cdot \frac{f(\chi_1)}{f(Z_s)}} \quad (3.6)$$

$$\vdots$$

$\chi_1,\ Z_{ref}$;
$$\frac{\frac{R(Z_{ref},\chi_1)}{R_z}}{\frac{R(Z_{ref},\chi_1)}{R_z}} = \frac{\frac{\varphi(Z_{ref})}{\varphi(0^\circ)}\cdot\frac{f(\chi_1)}{f(Z_s)}}{\frac{\varphi(Z_{ref})}{\varphi(0^\circ)}\cdot\frac{f(\chi_1)}{f(Z_s)}} \tag{3.7}$$

$$\vdots$$

$\chi_1,\ Z_8$;
$$\frac{\frac{R(Z_8,\chi_1)}{R_z}}{\frac{R(Z_{ref},\chi_1)}{R_z}} = \frac{\frac{\varphi(Z_8)}{\varphi(0^\circ)}\cdot\frac{f(\chi_1)}{f(Z_s)}}{\frac{\varphi(Z_{ref})}{\varphi(0^\circ)}\cdot\frac{f(\chi_1)}{f(Z_s)}} \tag{3.8}$$

From this, the $R(Z,\chi)$ function that only depends on the $\varphi(Z)/\varphi(0^\circ)$ function is proposed as below:

$\chi_1,\ Z_1$;
$$\frac{R(Z_1,\chi_1)}{R(Z_{ref},\chi_1)} = \frac{\varphi(Z_1)}{\varphi(Z_{ref})} \tag{3.9}$$

$\chi_1,\ Z_2$;
$$\frac{R(Z_2,\chi_1)}{R(Z_{ref},\chi_1)} = \frac{\varphi(Z_2)}{\varphi(Z_{ref})} \tag{3.10}$$

$$\vdots$$

$\chi_1,\ Z_{ref}$;
$$\frac{R(Z_{ref},\chi_1)}{R(Z_{ref},\chi_1)} = 1 \tag{3.11}$$

$$\vdots$$

$\chi_1,\ Z_8$;
$$\frac{R(Z_8,\chi_1)}{R(Z_{ref},\chi_1)} = \frac{\varphi(Z_8)}{\varphi(Z_{ref})} \tag{3.12}$$

Thirdly, the values of sky radiance from $R(Z_1,\chi_1)/R(Z_{ref},\chi_1)$ to $R(Z_8,\chi_1)/R(Z_{ref},\chi_1)$ corresponding to Equation (3.9) to Equation (3.12), which represent the intersections between each Z zone and χ zone were obtained from measurements taken by the EKO sky scanner. Consequently, the values from $\varphi(Z_1)/\varphi(Z_{ref})$ to $\varphi(Z_8)/\varphi(Z_{ref})$ can be estimated by plotting graphs, with Z_1 to Z_2 on the x-axis and the corresponding sky radiance values on the y-axis. In order to determine the value of the $\varphi(Z)/\varphi(0^\circ)$, the y-intercept of the plotted data is used. Similarly, the value of $\varphi(Z)/\varphi(0^\circ)$ at each χ_2 to χ_{30} can be obtained using the same approach. Following this methodology, the value of the $\varphi(Z)/\varphi(0^\circ)$ function depends on Z_s, Z, and n was analyzed across a range of sky conditions, from clear to overcast, as shown in Figure 8.

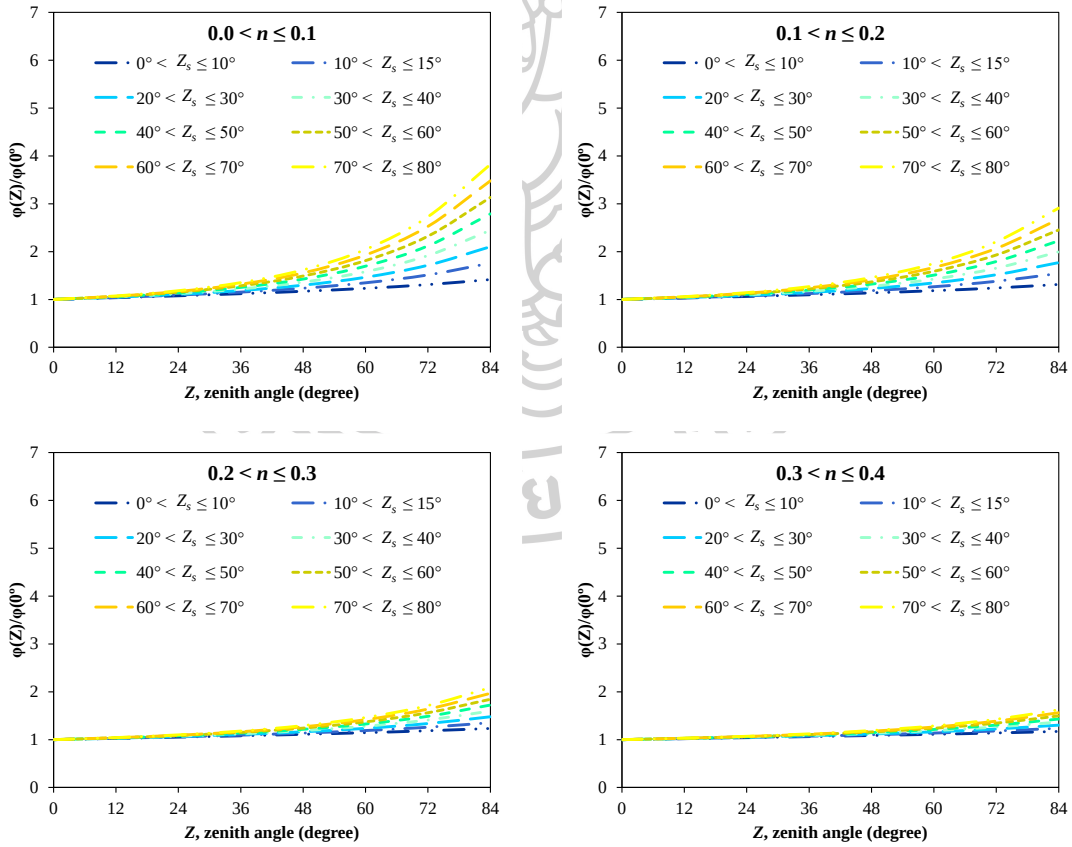

Figure 8 The plots of $\varphi(Z)/\varphi(0^\circ)$ function at various Z_s and Z according to n from clear sky to overcast sky conditions.

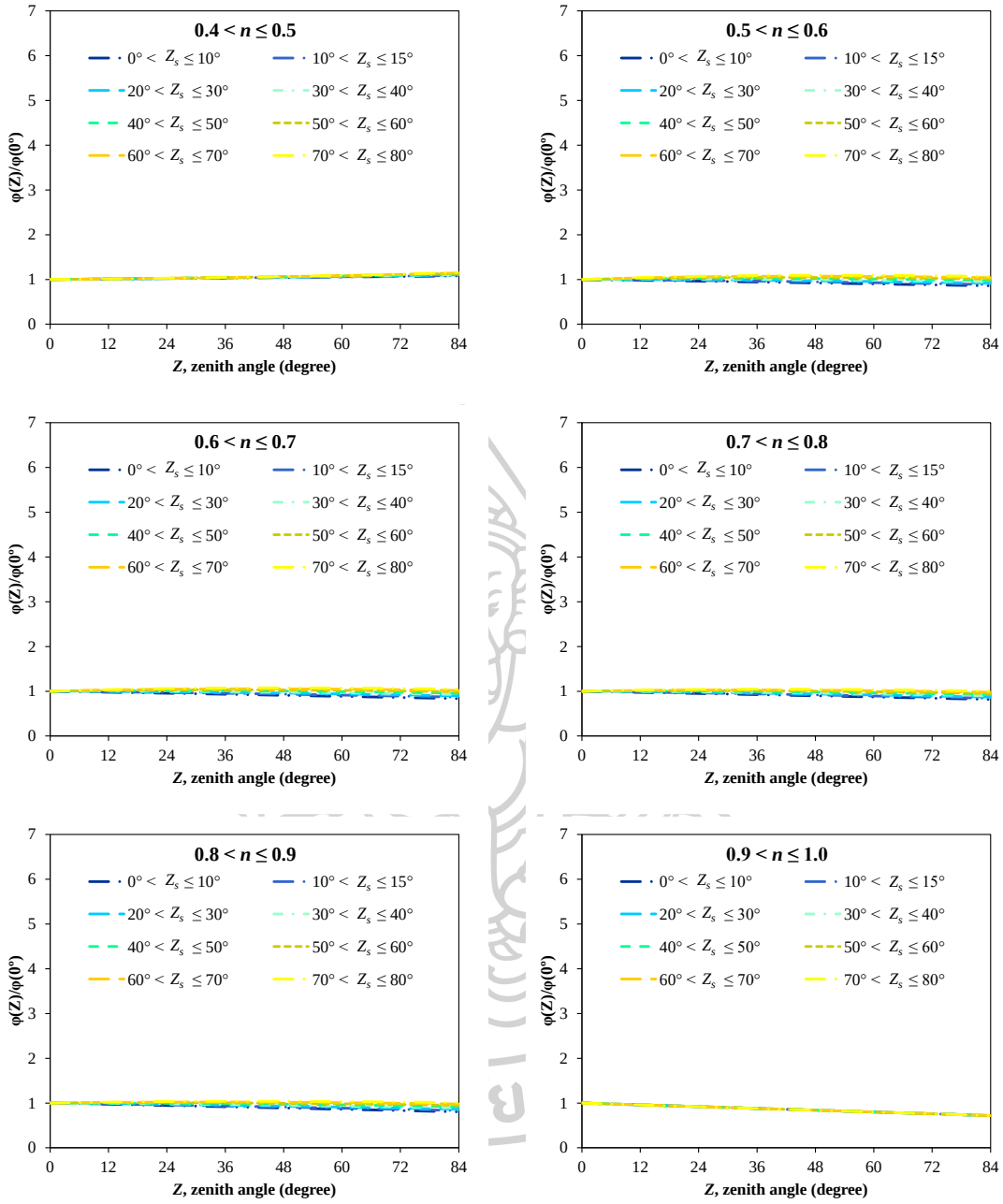

Figure 8 (continues).

Finally, the best-fitted curve representing the $\varphi(Z)/\varphi(0^{\circ})$ function as shown in Figure 8 was modeled using an exponential function, as expressed in Equation (3.13). The corresponding coefficients a_0 to a_4 were determined using Statistica software (version 10) and are listed in Table 8. In addition, the coefficient of determination

(R^2) is also provided in Table 8. An R^2 value close to 1 indicates a strong correlation in the model fit.

$$\frac{\varphi(Z)}{\varphi(0^\circ)} = 1 + a_0(Z)exp\left[\frac{a_1}{cos(a_2 Z)}\right] + a_3(Z)(Z_s)exp(a_4 Z) \quad (3.13)$$

where Z_s and Z are in radian.

Table 8 The empirical adjustable coefficients of Equation (3.13) for $\varphi(Z)/\varphi(0^\circ)$ function.

n	a_0	a_1	a_2	a_3	a_4	R^2
0.0 < n ≤ 0.1	0.15426	0.07125	0.00001	0.09796	1.78611	0.998
0.1 < n ≤ 0.2	0.12484	0.09865	0.00001	0.07748	1.66445	0.974
0.2 < n ≤ 0.3	0.10436	0.11025	0.00001	0.04832	1.56459	0.983
0.3 < n ≤ 0.4	0.08405	0.13088	0.00001	0.02956	1.46486	0.945
0.4 < n ≤ 0.5	0.04435	0.1508	0.00001	0.00985	1.00611	0.978
0.5 < n ≤ 0.6	-0.09463	0.13809	0.00001	0.27413	-0.5659	0.957
0.6 < n ≤ 0.7	-0.10463	0.14564	0.00001	0.25324	-0.52548	0.936
0.7 < n ≤ 0.8	-0.11463	0.15632	0.00001	0.21536	-0.49556	0.954
0.8 < n ≤ 0.9	-0.12299	0.16474	0.00001	0.19695	-0.36582	0.948
0.9 < n ≤ 1.0	-0.25592	0.20625	0.00001	0.05648	-0.22059	0.956

3) Eliminating the $\varphi(Z)/\varphi(0^\circ)$ function

Whereas the methodology used to eliminate the $\varphi(Z)/\varphi(0^\circ)$ function from the $f(\chi)/f(Z_s)$ function follows a similar approach to that used in the elimination of the $f(\chi)/f(Z_s)$ function from the $\varphi(Z)/\varphi(0^\circ)$ function, as outlined previously. However, this elimination differs in that, for a given Z zone, the variation of the Z zone is constant at different χ zone, Firstly, the formula for R/R_z was reformed

from Equation (1.16) into the form shown in Equation (3.14) to Equation (3.16), as defined below:

$Z_1,\ \chi_1;$ $$\frac{R(Z_1,\chi_1)}{R_z} = \frac{\varphi(Z_1)}{\varphi(0^\circ)} \cdot \frac{f(\chi_1)}{f(Z_s)} \tag{3.14}$$

$Z_1,\ \chi_2;$ $$\frac{R(Z_1,\chi_2)}{R_z} = \frac{\varphi(Z_1)}{\varphi(0^\circ)} \cdot \frac{f(\chi_2)}{f(Z_s)} \tag{3.15}$$

$$\vdots$$

$Z_1,\ \chi_{30};$ $$\frac{R(Z_1,\chi_{30})}{R_z} = \frac{\varphi(Z_1)}{\varphi(0^\circ)} \cdot \frac{f(\chi_{30})}{f(Z_s)} \tag{3.16}$$

The χ at χ_{15} was chosen for the reference formula ($\chi_{15} = \chi_{ref}$) as:

$Z_1,\ \chi_1;$ $$\frac{\frac{R(Z_1,\chi_1)}{R_z}}{\frac{R(Z_1,\chi_{ref})}{R_z}} = \frac{\frac{\varphi(Z_1)}{\varphi(0^\circ)} \cdot \frac{f(\chi_1)}{f(Z_s)}}{\frac{\varphi(Z_1)}{\varphi(0^\circ)} \cdot \frac{f(\chi_{ref})}{f(Z_s)}} \tag{3.17}$$

$Z_1,\ \chi_2;$ $$\frac{\frac{R(Z_1,\chi_2)}{R_z}}{\frac{R(Z_1,\chi_{ref})}{R_z}} = \frac{\frac{\varphi(Z_1)}{\varphi(0^\circ)} \cdot \frac{f(\chi_2)}{f(Z_s)}}{\frac{\varphi(Z_1)}{\varphi(0^\circ)} \cdot \frac{f(\chi_{ref})}{f(Z_s)}} \tag{3.18}$$

$$\vdots$$

$Z_1,\ \chi_{ref};$ $$\frac{\frac{R(Z_1,\chi_{ref})}{R_z}}{\frac{R(Z_1,\chi_{ref})}{R_z}} = \frac{\frac{\varphi(Z_1)}{\varphi(0^\circ)} \cdot \frac{f(\chi_{ref})}{f(Z_s)}}{\frac{\varphi(Z_1)}{\varphi(0^\circ)} \cdot \frac{f(\chi_{ref})}{f(Z_s)}} \tag{3.19}$$

$$\vdots$$

$$Z_1,\ \chi_{30}; \qquad \frac{\dfrac{R(Z_1,\chi_{30})}{R_z}}{\dfrac{R(Z_1,\chi_{ref})}{R_z}} = \frac{\dfrac{\varphi(Z_1)}{\varphi(0^\circ)}\cdot\dfrac{f(\chi_{30})}{f(Z_s)}}{\dfrac{\varphi(Z_1)}{\varphi(0^\circ)}\cdot\dfrac{f(\chi_{ref})}{f(Z_s)}} \tag{3.20}$$

With this step, the $\varphi(Z)/\varphi(0^\circ)$ function can be canceled out by dividing the reference formula, leading us to the following results:

$$Z_1,\ \chi_1; \qquad \frac{R(Z_1,\chi_1)}{R_{ref}(Z_1,\chi_{ref})} = \frac{f(\chi_1)}{f(\chi_{ref})} \tag{3.21}$$

$$Z_1,\ \chi_2; \qquad \frac{R(Z_1,\chi_2)}{R_{ref}(Z_1,\chi_{ref})} = \frac{f(\chi_2)}{f(\chi_{ref})} \tag{3.22}$$

$$\vdots$$

$$Z_1,\ \chi_{ref}; \qquad \frac{R_{ref}(Z_1,\chi_{ref})}{R_{ref}(Z_1,\chi_{ref})} = 1 \tag{3.23}$$

$$\vdots$$

$$Z_1,\ \chi_{30}; \qquad \frac{R(Z_1,\chi_{30})}{R_{ref}(Z_1,\chi_{ref})} = \frac{f(\chi_{30})}{f(\chi_{ref})} \tag{3.24}$$

Secondly, since the χ represents the angular distance between the sun and a given point in the sky, even though the Z_s changes, the distance of a given point in the sky remains constant. In other words, the χ independent of Z_s (Janjai et al., 2008). Then, the values of $f(\chi)/f(\chi_{ref})$ were plotted against the values of χ without Z_s, and the results are shown in Figure 9.

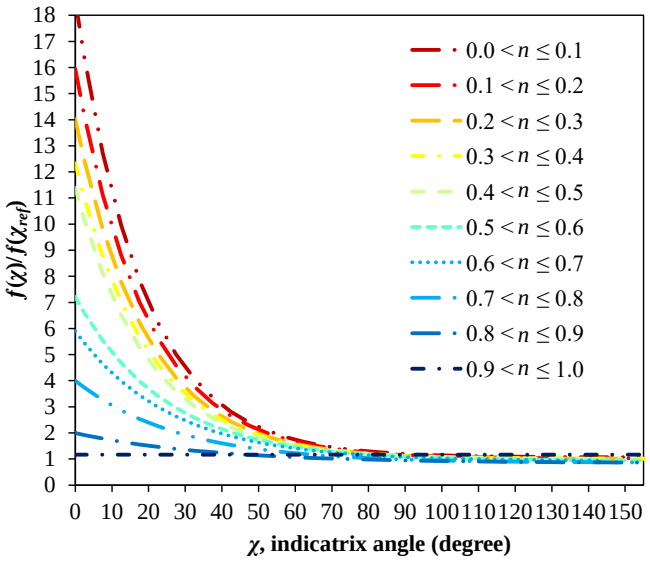

Figure 9 Plots of $f(\chi)/f(\chi_{ref})$ function at various χ from clear sky to overcast sky conditions.

Thirdly, an empirical relationship based on Figure 9 can be expressed as follows:

$$\frac{f(\chi)}{f(\chi_{ref})} = b_0 + b_1 exp(b_2 \chi) \tag{3.25}$$

The corresponding coefficients b_0 to b_2 are listed in Table 9.

To provide the Z_s in $f(\chi)/f(Z_s)$ function can be obtained by replacing χ for Z_s in Equation (3.25).

$$\frac{f(Z_s)}{f(\chi_{ref})} = b_0 + b_1 exp(b_2 Z_s) \tag{3.26}$$

Finally, by dividing Equation (3.25) by Equation (3.26), we obtain the $f(\chi)/f(Z_s)$ function as:

$$\frac{f(\chi)}{f(Z_s)} = \frac{b_0 + b_1 exp(b_2 \chi)}{b_0 + b_1 exp(b_2 Z_s)} \tag{3.27}$$

Table 9 The empirical adjustable coefficients of Equation (3.27) for $f(\chi)/f(Z_s)$ function.

n	b_0	b_1	b_2	R^2
0.0 < n ≤ 0.1	1.06240	17.51529	-3.10628	0.998
0.1 < n ≤ 0.2	1.01663	14.93120	-2.98272	0.997
0.2 < n ≤ 0.3	1.00650	13.01253	-2.98670	0.996
0.3 < n ≤ 0.4	1.00637	11.32651	-2.89810	0.997
0.4 < n ≤ 0.5	1.00613	10.37982	-2.89660	0.995
0.5 < n ≤ 0.6	0.93557	6.27536	-2.36258	0.995
0.6 < n ≤ 0.7	0.92553	4.97587	-2.23547	0.998
0.7 < n ≤ 0.8	0.85634	3.14567	-2.06087	0.987
0.8 < n ≤ 0.9	0.84699	1.14584	-1.56036	0.997
0.9 < n ≤ 1.0	0.81463	0.35414	-0.2543	0.998

4) Combination of the $\varphi(Z)/\varphi(0^\circ)$ function with the $f(\chi)/f(Z_s)$ function for calculating R/R_z

Overall, the R/R_z proposed in this study can be considered by combining the $\varphi(Z)/\varphi(0^\circ)$ function from Equation (3.13) with the $f(\chi)/f(Z_s)$ function from Equation (3.27), resulting in:

$$\frac{R}{R_z} = \left\{1 + a_0(Z)exp\left[\frac{a_1}{cos(a_2 Z)}\right] + a_3(Z)(Z_s)exp(a_4 Z)\right\} \times \left\{\frac{b_0 + b_1 exp(b_2 \chi)}{b_0 + b_1 exp(b_2 Z_s)}\right\} \quad (3.28)$$

The distribution of R/R_z of 10 sky conditions according to the n, when the Z_s is 35° and ϕ_s is 270°, is shown in Figure 10.

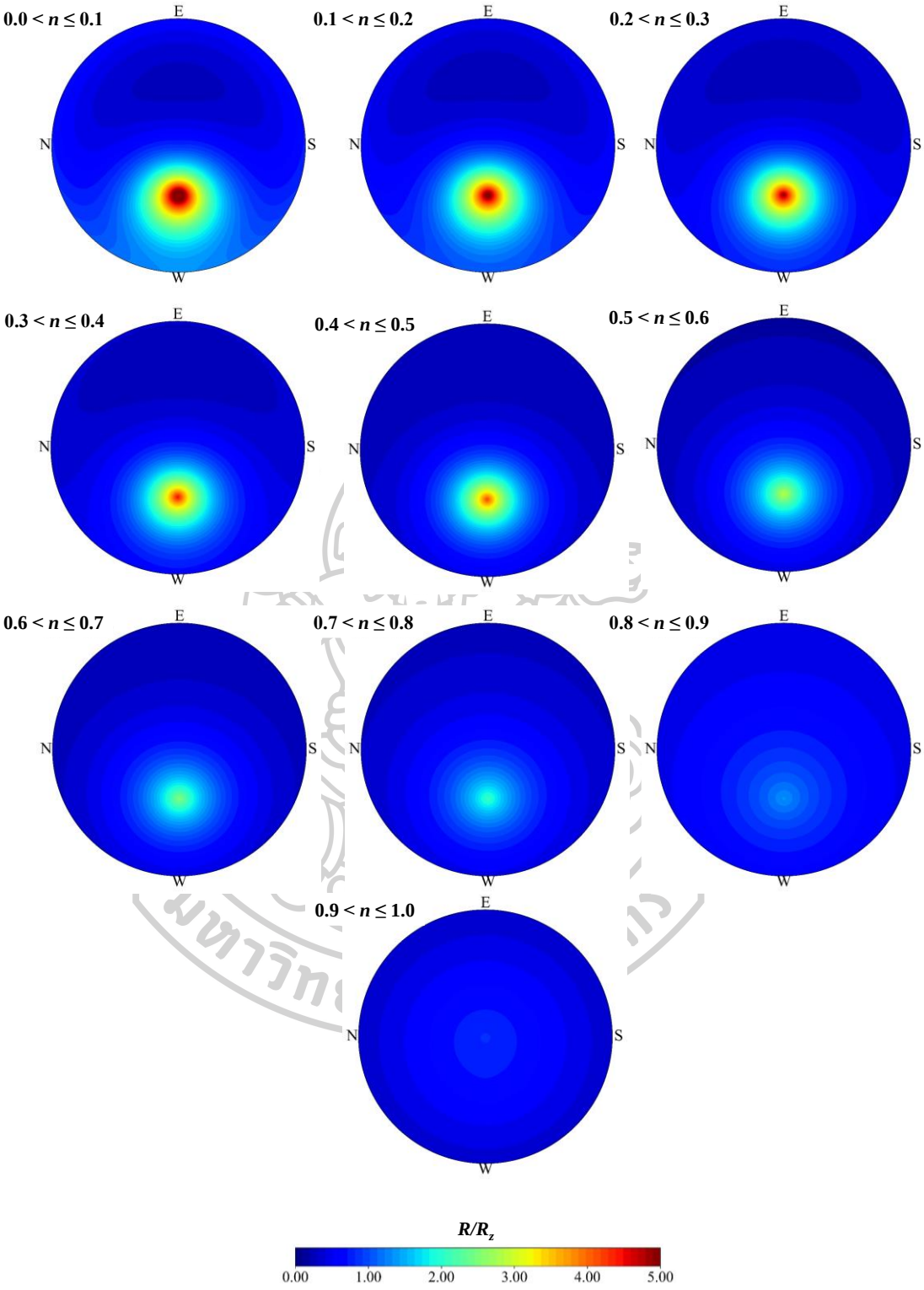

Figure 10 The distribution of R / R_z of 10 sky conditions according to n from clear to overcast sky condition.

3.2.4 Statistical error

Accuracy is the most significant criterion for validating the performance success of calculation methods. To assess the accuracy of a model, we selected the root mean square error ($RMSE$) and the mean bias error (MBE), both expressed as percentages (%), as statistical error measures. These mathematical are calculated by using the following Equations:

$$RMSE = \frac{\sqrt{\frac{1}{N}\sum_{i=1}^{N}\left[(R/R_z)_{i,mod} - (R/R_z)_{i,meas}\right]^2}}{\frac{1}{N}\sum_{i=1}^{N}\left[(R/R_z)_{i,meas}\right]} \times 100 \quad (3.29)$$

$$MBE = \frac{\frac{1}{N}\sum_{i=1}^{N}\left[(R/R_z)_{i,mod} - (R/R_z)_{i,meas}\right]}{\frac{1}{N}\sum_{i=1}^{N}\left[(R/R_z)_{i,meas}\right]} \times 100 \quad (3.30)$$

where $(R/R_z)_{i,mod}$ is the data of sky radiance calculated from the model, $(R/R_z)_{i,meas}$ is the data of sky radiance measured from an EKO sky scanner, N is the total number of data.

3.3 Results and discussion

3.3.1 Validation of the model

To evaluate the proposed model across 10 sky conditions, statistical errors were calculated for each condition and station, as summarized in Table 10. Analysis of three typical sky types (clear, intermediate, overcast) shows the model performs best under clear skies ($0.0 < n \leq 0.1$) with errors ranging from 27.29% to 31.96%, followed by overcast ($0.9 < n \leq 1.0$; 28.04%–32.46%), and intermediate conditions ($0.4 < n \leq 0.5$; 34.36%–40.05%), as indicated by $RMSE$ values under all stations. Higher accuracy under clear skies is due to stable atmospheric conditions, while heterogeneous clouds in intermediate skies cause greater uncertainty. Although both clear and overcast skies are stable, overcast conditions show slightly higher errors

due to varying cloud properties. The model tends to overestimate under clear skies and underestimate under intermediate and overcast skies. The $RMSE$ values under different sky conditions, which are around 30%, are consistent with those reported in previous studies, such as Gracia et al. (Gracia et al., 2011), suggesting that 20-30% of $RMSE$ is typical for sky models. A comparison of the proposed model with existing sky models will be presented in the next section to further illustrate these errors.

Table 10 Summary statistics between calculated and measured R / R_z under different sky conditions and stations.

n	Station	$RMSE$ (%)	MBE (%)
$0.0 < n \leq 0.1$	Chiang Mai	27.29	3.02
	Ubon Ratchathani	29.76	10.07
	Nakhon Pathom	28.63	7.67
	Songkhla	31.97	3.43
$0.1 < n \leq 0.2$	Chiang Mai	31.43	5.97
	Ubon Ratchathani	26.97	5.15
	Nakhon Pathom	30.06	3.55
	Songkhla	32.94	8.27
$0.2 < n \leq 0.3$	Chiang Mai	34.68	1.08
	Ubon Ratchathani	28.19	-3.35
	Nakhon Pathom	31.49	1.61
	Songkhla	33.93	-4.96
$0.3 < n \leq 0.4$	Chiang Mai	39.87	0.12
	Ubon Ratchathani	33.40	-5.57
	Nakhon Pathom	32.93	-4.74
	Songkhla	34.90	-7.64

Table 10 (continues)

n	Station	$RMSE$ (%)	MBE (%)
$0.4 < n \leq 0.5$	Chiang Mai	40.06	-2.17
	Ubon Ratchathani	35.60	-7.77
	Nakhon Pathom	34.36	-8.87
	Songkhla	35.89	-10.33
$0.5 < n \leq 0.6$	Chiang Mai	39.87	-2.88
	Ubon Ratchathani	37.57	-7.73
	Nakhon Pathom	33.57	-7.91
	Songkhla	34.12	-10.13
$0.6 < n \leq 0.7$	Chiang Mai	36.68	-3.61
	Ubon Ratchathani	35.54	-7.69
	Nakhon Pathom	32.76	-6.96
	Songkhla	32.34	-9.91
$0.7 < n \leq 0.8$	Chiang Mai	33.50	-4.32
	Ubon Ratchathani	36.52	-7.63
	Nakhon Pathom	31.96	-6.03
	Songkhla	30.59	-9.70
$0.8 < n \leq 0.9$	Chiang Mai	30.31	-5.05
	Ubon Ratchathani	33.50	-7.59
	Nakhon Pathom	31.15	-5.08
	Songkhla	28.82	-9.48
$0.9 < n \leq 1.0$	Chiang Mai	29.11	-5.77
	Ubon Ratchathani	32.47	-7.55
	Nakhon Pathom	30.36	-4.12
	Songkhla	28.04	-9.26

3.3.2 Comparison with existing sky models

To better evaluate the proposed model, we compared it with EKO sky scanner measurements and existing sky models (CIE, Igawa, and CIE-NASR) at Nakhon Pathom station from November 2023 to October 2024. Coefficients for the CIE and CIE-NASR models were assigned using visual sky observations, while the S_i value classified sky types for the Igawa model. As shown in Table 11, under clear skies ($0.0 < n \leq 0.1$), the proposed model had the lowest error (28.628%), slightly outperforming the CIE model (29.694%). Under intermediate skies ($0.4 < n \leq 0.5$), the proposed model again achieved the best result (34.360%). Under overcast skies ($0.9 < n \leq 1.0$), the Igawa model performed best (27.361%), while the proposed model showed slightly higher error (30.359%). The Igawa model's low error under overcast skies is attributed to its ability to account for cloud scattering variations. Overall, the proposed model showed consistent and reliable performance across all sky conditions, confirming its ability to calculate and assess sky radiance from satellite data.

Table 11 Summary statistics error of four sky models with measured R / R_z under three different sky conditions comparison case study at Nakhon Pathom station.

n	Model	$RMSE$ (%)	MBE (%)
$0.0 < n \leq 0.1$	CIE	29.69	7.23
	CIE-NASR	30.97	12.46
	Igawa	33.44	9.89
	Proposed	28.63	7.67
$0.1 < n \leq 0.2$	CIE	32.93	6.01
	CIE-NASR	33.13	9.41
	Igawa	35.38	8.01
	Proposed	30.06	3.55

Table 11 (continues)

n	Model	$RMSE$ (%)	MBE (%)
$0.0 < n \leq 0.1$	CIE	29.69	7.23
	CIE-NASR	30.97	12.46
	Igawa	33.44	9.89
	Proposed	28.63	7.67
$0.1 < n \leq 0.2$	CIE	32.93	6.01
	CIE-NASR	33.13	9.41
	Igawa	35.38	8.01
	Proposed	30.06	3.55
$0.2 < n \leq 0.3$	CIE	36.16	4.80
	CIE-NASR	35.28	6.37
	Igawa	37.32	7.56
	Proposed	31.49	1.61
$0.3 < n \leq 0.4$	CIE	39.39	3.58
	CIE-NASR	37.43	3.32
	Igawa	39.26	6.13
	Proposed	32.93	-4.74
$0.4 < n \leq 0.5$	CIE	42.62	2.37
	CIE-NASR	39.58	0.26
	Igawa	41.20	5.05
	Proposed	34.36	-8.87
$0.5 < n \leq 0.6$	CIE	40.34	2.96
	CIE-NASR	37.80	1.71
	Igawa	38.43	6.56
	Proposed	33.57	-7.91
$0.6 < n \leq 0.7$	CIE	38.07	3.57
	CIE-NASR	36.03	3.14
	Igawa	35.67	10.78

Table 11 (continues)

n	Model	$RMSE$ (%)	MBE (%)
$0.6 < n \leq 0.7$	Proposed	32.76	-6.96
$0.7 < n \leq 0.8$	CIE	35.79	4.16
	CIE-NASR	34.24	4.58
	Igawa	32.91	10.23
	Proposed	31.96	-6.03
$0.8 < n \leq 0.9$	CIE	33.52	4.76
	CIE-NASR	32.46	6.01
	Igawa	30.13	11.57
	Proposed	31.15	-5.08
$0.9 < n \leq 1.0$	CIE	31.23	5.36
	CIE-NASR	30.68	7.45
	Igawa	27.36	15.30
	Proposed	30.36	-4.12

3.4 Conclusions

This study proposes an empirical model for identifying sky conditions using a cloud index (n) derived from satellite data to calculate relative sky radiance (R / R_z) under different geographical and climatic characteristics in the tropical environment of Thailand. The empirical adjustable coefficients for the proposed model were established using five years of average measured sky radiance data at Nakhon Pathom station. To validate the model, sky radiance measurement data at four main regions in Thailand namely Chiang Mai, Ubon Ratchathani, Songkhla, and Nakhon Pathom were analyzed under clear, intermediate, overcast as well as all sky conditions. A statistical error analysis indicated that the model performed optimally under clear sky conditions, obtaining the lowest $RMSE$ values when compared to intermediate and overcast conditions. Under different sky conditions, the $RMSE$ values of the proposed model were around 30%. While the empirical adjustable

coefficients were derived specifically from one station, a comparison of data from the four measurement locations at different climatic regions in Thailand demonstrated that the coefficients of the empirical model are not dependent on the location.

Chapter 4

Analysis of zenith sky radiance in the tropics: A case study of Chiang Mai and Nakhon Pathom, Thailand*

4.1 Introduction

Zenith sky radiance (R_z) is a part of the model that is used to convert relative sky radiance (R / R_z) to absolute sky radiance (R). Some works have been studied to estimate R_z. For example, the study at a high latitude in Pamplona, Spain (Torres et al., 2010) revealed that the R_z varies with solar altitude (α_s) and sky conditions. In contrast with Spain, Thailand is located in a tropical area where the environment is quite different from high latitudes. Hence, this study has two main objectives. The first objective is to analyze in detail of the diurnal and seasonal variations of the R_z under all sky conditions with different two measurement stations located in the tropics. The second objective is to develop a model of the R_z under clear sky condition as a function of α_s.

4.2 Data and methods

The ground-based measurements of the R_z data and clear sky identification were conducted at two stations located in a tropical environment, Thailand namely Chiang Mai station (18.78°N, 98.98°E) and Nakhon Pathom station (13.82°N, 100.04°E) as shown in Figure 10. In this study, data collected from both sites during 8:00 to 16:00 at local time were used. The details of instruments used in this study and the methodology are as follows.

4.2.1 Zenith sky radiance data

A sky scanner (model: MS-321LR) (Figure 11), which was calibrated and manufactured by EKO company in Japan is used to collect R_z data at both stations. Sky scanners employ two different sensors consisting of sky radiance and sky

* This paper has been published to Current Applied Science and Technology (Q4).

luminance over 145 points (shown in Figure 12) covering the sky dome, located in a two-axis tracking system for the required azimuth angles and altitude angles. For sky scanning sequence number 145 (Figure 13) was considered the zenith sky radiance which was used in this study.

Figure 11 Map of Thailand showing the locations at Chiang Mai station and Nakhon Pathom station and measurements together with the elevation.

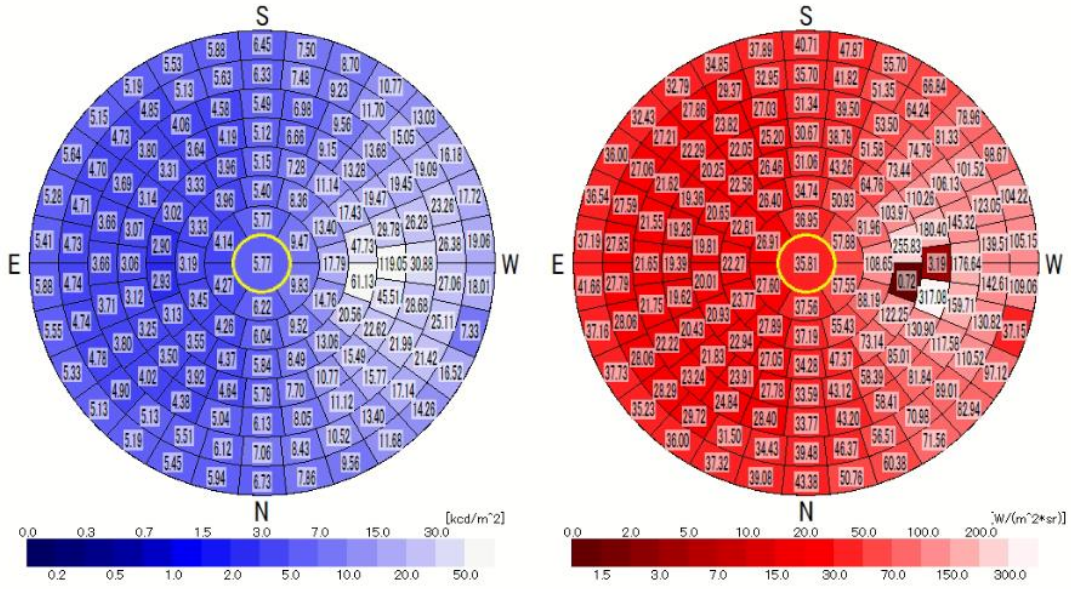

(a) (b)

Figure 12 Examples of sky luminance (a) and sky radiance (b) from the EKO sky scanner.

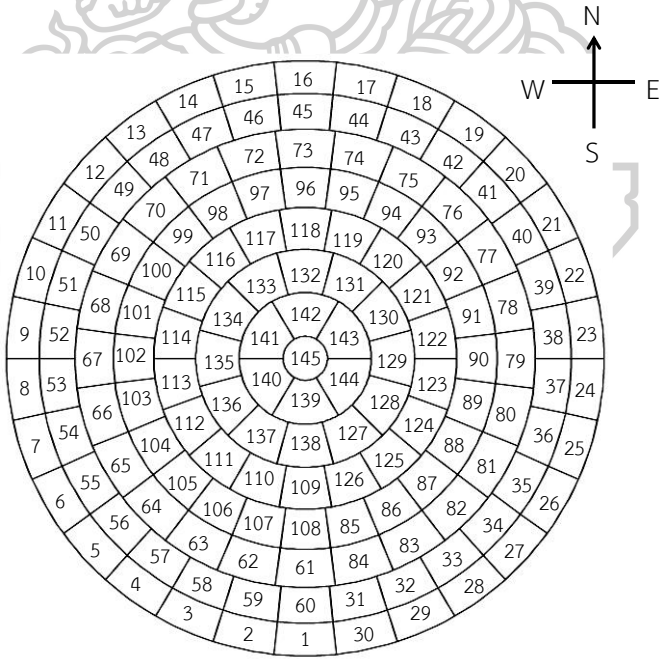

Figure 13 The 145 measurement points of the EKO sky scanner.

4.2.2 Clear sky identification

Sky images obtained from the sky camera (model: PSV-100) of PREDE company in Japan and the sky camera (model: ASI-16) of EKO company in Japan (Figure 11) were taken every 30 minutes to correspond with the sky scanner and were used to identify the clear sky. These cameras are automatic cameras with a fish eye objective and 180° field of view that captures images of the sky. To identify the R_z under clear sky condition, the image as very clear with no clouds were used and these images were selected by human observation. A sample of the image with a clear sky used in this study can be seen in Figure 14.

Figure 14 An example of sky image under clear sky condition from the EKO sky camera.

4.2.3 Formulation of the model

In the last decade, some research efforts have been focused on developing mathematical models of hourly R_z as a function of α_s with 3rd-degree polynomials (Soler and Gopinathan, 2004). This study concentrates on the estimation of hourly R_z under clear sky condition due to easy to model (cancel out the effect of clouds) and the maximum electric conversion of the PV panels was carried out by solar irradiance under clear sky condition. R_z collected from Nakhon Pathom station in

2016 was employed to determine the parameter of model adjustments. The relationship between hourly R_z and α_s is shown in Figure 15.

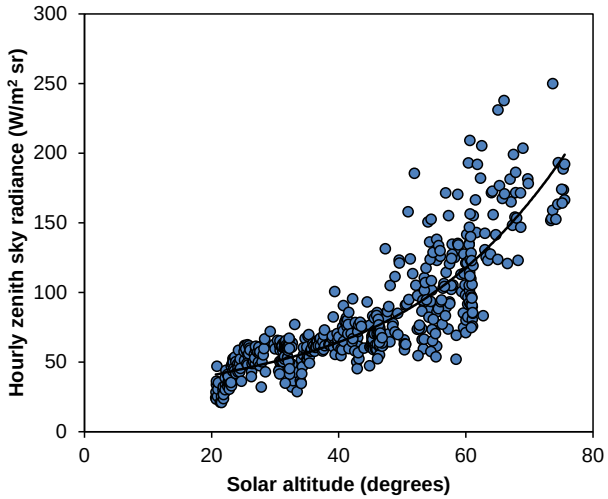

Figure 15 The relationship between hourly R_z under clear sky condition and α_s.

From Figure 15, the best fit with 3rd-degree polynomial was established as follows:

$$R_z = 0.0008\alpha_s^3 - 0.0690\alpha_s^3 + 2.9288\alpha_s - 10.5170 \quad (4.1)$$

4.2.4 Validation of the model

The R_z measured at Chiang Mai station in 2016 and Nakhon Pathom station between August 2023 and September 2024 were used for model validation. There are indicators that represent mathematical model accuracy. $RMSE$ and MBE according to Equations (3.29) and (3.30), respectively, were employed for validation of the model's accuracy.

4.3 Results and discussion

4.3.1 Diurnal variation of zenith sky radiance

The monthly average hourly of R_z under all sky conditions at two stations in 2016 is shown in Figure 16. We only present a curve for 8:00–9:00 (representing morning), 12:00–13:00 (representing noon), and 15:00–16:00 (representing afternoon). It can be seen from Figure 16 that the R_z at both sites increases from the morning to reach the peak at noon and then decreases in the afternoon according to sun position in terms of α_s. The α_s varies on the time of the day. Every day, the α_s is equal to 0° when the sun rises and increases to 90° around noon then decreases to 0° again when the sun sets.

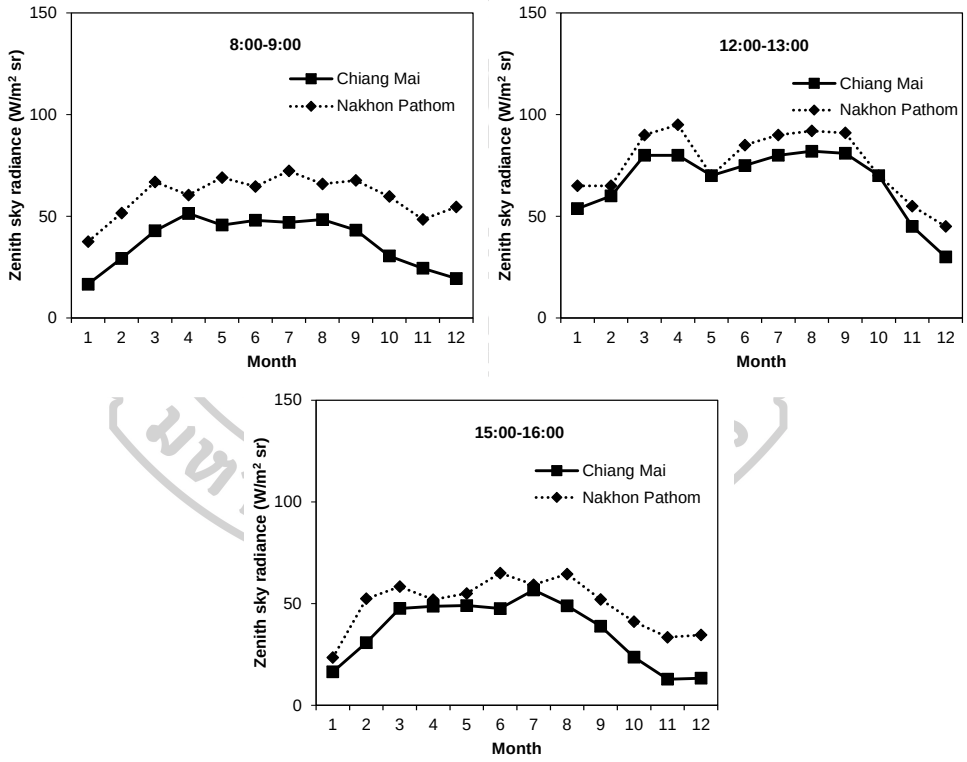

Figure 16 Monthly average hourly R_z for morning (8:00-9:00), noon (12:00-13:00), and afternoon (15:00-16:00).

4.3.2 Seasonal variation of zenith sky radiance

Figure 17 illustrates the monthly average daily variation in R_z for 2016, highlighting its seasonal changes. The results from both stations show similar patterns across the different seasons, which are driven by the sun's declination. As the Earth orbits the sun, its axial tilt causes the sun's position in the sky to shift, leading to seasonal variations. During the summer (mid-February to mid-May) and rainy season (mid-May to mid-October), the sun's declination is around 0 degrees. However, R_z is higher in summer due to clearer skies, while cloud cover, which reduces the R_z, can be seen in the rainy season. In winter (mid-October to mid-February), when the sun's declination reaches -23.5 degrees, the lowest R_z is observed as the sun is lower in the sky. In addition to solar declination, the latitude of the measurement site plays a role in R_z. Nakhon Pathom, located at a lower latitude, records the highest values, while Chiang Mai, at a higher latitude, shows the lowest values. Thus, R_z is affected by solar declination, cloud cover, and the location's latitude.

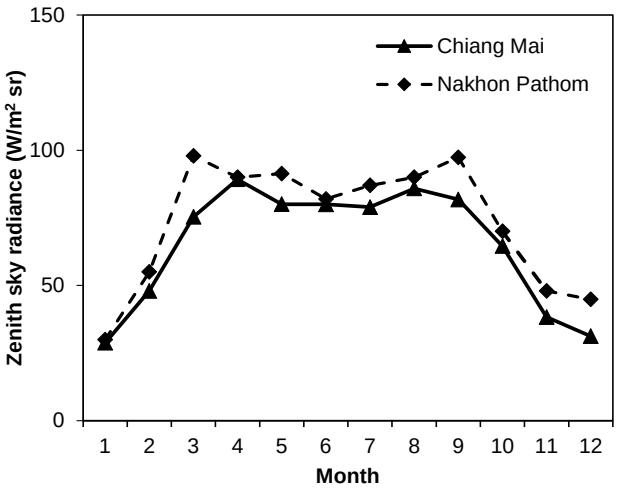

Figure 17 Monthly average daily R_z.

4.3.3 Validation result

The hourly R_z under clear sky condition at Chiang Mai station obtained from the model was compared with the hourly R_z under clear sky condition data from

measurements. However, the data obtained from Chiang Mai station in 2016 represents historical measurements. Therefore, R_z data collected from Nakhon Pathom station between August 2023 and September 2024 were included for comparison. The result of the comparison is shown in Figure 18. It can be observed that the hourly R_z under clear sky condition from the model are in reasonable agreement with the data from the measurement, with $RMSE$ of 30.17% and overestimated with MBE of 7.48%.

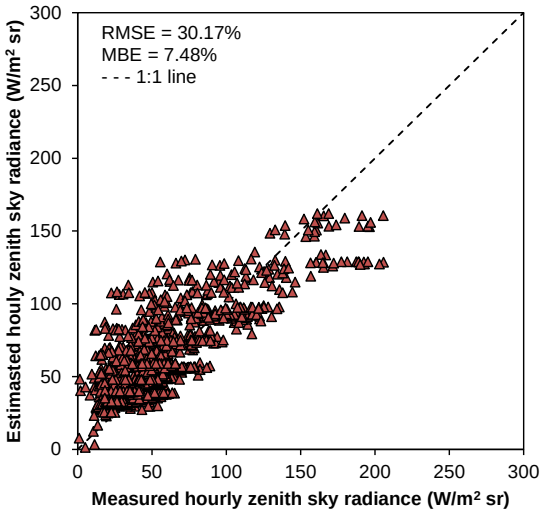

Figure 18 Comparison of the measured hourly R_z under clear sky condition versus the estimated hourly R_z under clear sky condition from the model.

4.4 Conclusions

Thailand is situated in a tropical environment characterized by rapid cloud movement. This study analyzes the diurnal and seasonal variations of zenith sky radiance (R_z) measured by a sky scanner under all sky conditions at two sites: Chiang Mai station and Nakhon Pathom station in Thailand, during 2016. The diurnal variations of the R_z increased in the morning, peaked at noon, and decreased in the afternoon. The most significant seasonal variation in R_z is observed during the summer months of mid-February to mid-May, when radiance levels are at their highest. Conversely, the lowest values are recorded during the winter season, from

mid-October to mid-February. The analyses also indicate that solar altitude (α), latitude, and cloud cover significantly affect these variations. Additionally, hourly R_z under clear sky conditions was estimated as a function of α. The measurement data at Nakhon Pathom station were used for model development. The hourly R_z under clear sky condition data collected at Chiang Mai and also Nakhon Pathom stations were employed to validate the accuracy of the model. The accuracy of the model showed reasonable agreement, with a root mean square error ($RMSE$) of 30.17% and a mean bias error (MBE) of 7.48%.

Chapter 5

Conclusions

This study has two objectives. First, to develop an empirical model for calculating relative sky radiance under different sky and climate conditions in the tropical climate of Thailand using geostationary satellite imagery. Second, to develop an empirical model for calculating zenith sky radiance under clear sky conditions: a case study of Chiang Mai and Nakhon Pathom, Thailand. The key conclusions of this study are as follows:

1) A model for identifying sky conditions using a cloud index (n) derived from satellite data to calculate relative sky radiance (R / R_z) under various geographical and climatic conditions in the tropical environment of Thailand has been developed. The empirical adjustable coefficients for the proposed model were established using five years of averaged sky radiance data from the Nakhon Pathom station. To validate the model, sky radiance measurement data from four major regions of Thailand, Chiang Mai, Ubon Ratchathani, Songkhla, and Nakhon Pathom, were analyzed under clear, intermediate, overcast, and all sky conditions. Statistical error analysis indicated that the model performed best under clear sky conditions, obtaining the lowest root mean square error ($RMSE$) values compared to intermediate and overcast conditions. Across different sky conditions, the $RMSE$ values of the proposed model were approximately 30%. Importantly, although the empirical coefficients were derived from a single site, the comparison of performance across regions with diverse climatic characteristics demonstrated that the model's coefficients are not location-dependent, confirming its broader applicability across different areas of Thailand.

2) An empirical model for estimating hourly zenith sky radiance (R_z) under clear sky conditions as a function of solar altitude (α) was developed, using data from Chiang Mai and Nakhon Pathom as a case study. The formula relationship between hourly R_z and α was characterized at the Nakhon Pathom station To validate the performance of the model, the hourly R_z measurements at Chiang Mai and Nakhon Pathom were employed. The model demonstrated reasonable accuracy, with an $RMSE$ of 30.17% and a mean bias error (MBE) of 7.48%. This result suggests that solar altitude plays a dominant role in determining zenith sky radiance under clear sky conditions in tropical environments, and that the model can effectively predict hourly variations in zenith sky radiance based on solar position.

By accurately estimating the distribution of sky radiance under different sky and climatic conditions, the model helps improve the prediction of solar energy availability on vertical and inclined surfaces, supporting the development of energy-efficient and sustainable architectural designs in tropical regions.

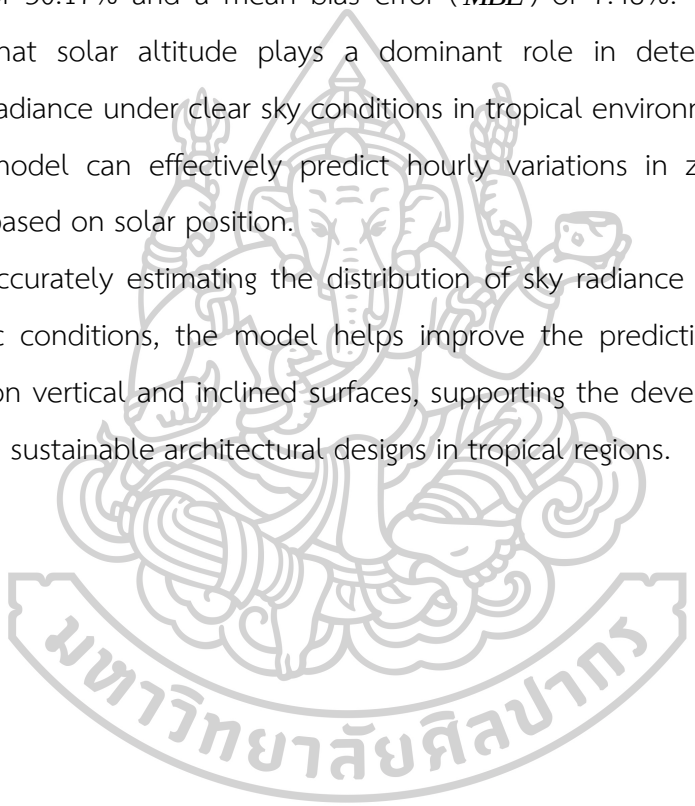

REFERENCES

Brunger, A. P., & Hooper, F. C. (1993). Anisotropic sky radiance model based on narrow field of view measurements of shortwave radiance. *Solar energy, 51*(1), 53-64.

Cano, D., Monget, J.-M., Albuisson, M., Guillard, H., Regas, N., & Wald, L. (1986). A method for the determination of the global solar radiation from meteorological satellite data. *Solar energy, 37*(1), 31-39.

Chirarattananon, S., & Chaiwiwatworakul, P. (2007). Distributions of sky luminance and radiance of North Bangkok under standard distributions. *Renewable Energy, 32*(8), 1328-1345.

CIE, S. (2003). Spitial distribution of daylight-cie stndard general sky. *CIE S 011.1/E*.

de Simón-Martín, M., Alonso-Tristán, C., & Díez-Mediavilla, M. (2017). Diffuse solar irradiance estimation on building's façades: review, classification and benchmarking of 30 models under all sky conditions. *Renewable and Sustainable Energy Reviews, 77*, 783-802.

Drif, M., Perez, P., Aguilera, J., & Aguilar, J. (2008). A new estimation method of irradiance on a partially shaded PV generator in grid-connected photovoltaic systems. *Renewable Energy, 33*(9), 2048-2056.

García-Rodríguez, A., García-Rodríguez, S., Díez-Mediavilla, M., & Alonso-Tristán, C. (2020). Photosynthetic active radiation, solar irradiance and the CIE standard sky classification. *Applied Sciences, 10*(22), 8007.

George, G., Wilson, R., & Joy, J. (2017). Ultraviolet spectroscopy: a facile approach for the characterization of nanomaterials. In *Spectroscopic methods for nanomaterials characterization* (pp. 55-72): Elsevier.

Goswami, D. Y. (2022). *Principles of solar engineering*: CRC press.

Gracia, A., Torres, J., De Blas, M., García, A., & Perez, R. (2011). Comparison of four luminance and radiance angular distribution models for radiance estimation. *Solar energy, 85*(9), 2202-2216.

Gueymard, C. A., & Kocifaj, M. (2022). Clear-sky spectral radiance modeling under variable aerosol conditions. *Renewable and Sustainable Energy Reviews, 168*,

112901.

Hammer, A., Heinemann, D., Hoyer, C., Kuhlemann, R., Lorenz, E., Müller, R., & Beyer, H. G. (2003). Solar energy assessment using remote sensing technologies. *Remote Sensing of Environment, 86*(3), 423-432.

Hess, S. (2014). Low-concentrating, stationary solar thermal collectors for process heat generation. *De Montfort University.*

Igawa, N., Koga, Y., Matsuzawa, T., & Nakamura, H. (2004). Models of sky radiance distribution and sky luminance distribution. *Solar energy, 77*(2), 137-157.

Ineichen, P., & Molineaux, B. (1993). *Characterisation and comparison of two sky scanners: PRC Krochmann and EKO instruments.* Paper presented at the Internal report, Groupe of Applied Physics, University of Geneva, Switzerland.

Janjai, S., Jantarach, T., & Laksanaboonsong, J. (2003). A model for calculating global illuminance from satellite data. *Renewable Energy, 28*(15), 2355-2365.

Janjai, S., Masiri, I., Nunez, M., & Laksanaboonsong, J. (2008). Modeling sky luminance using satellite data to classify sky conditions. *Building and Environment, 43*(12), 2059-2073.

Kittler, R. (1967). *Standardisation of outdoor con-ditions for the calculation of daylight factor with clear skies, in" Sunlight in Buildings.* Paper presented at the CIE 1965 Conference Proceedings.

Li, D. H., & Cheung, G. H. (2005). Study of models for predicting the diffuse irradiance on inclined surfaces. *Applied Energy, 81*(2), 170-186.

Li, D. H., & Lam, J. C. (2004). Predicting solar irradiance on inclined surfaces using sky radiance data. *Energy Conversion and Management, 45*(11-12), 1771-1783.

Li, D. H., & Lam, T. N. (2007). Determining the optimum tilt angle and orientation for solar energy collection based on measured solar radiance data. *International Journal of Photoenergy, 2007*(1), 085402.

Li, D. H., Lou, S., Lam, J. C., & Wu, R. H. (2016). Determining solar irradiance on inclined planes from classified CIE (International Commission on Illumination) standard skies. *Energy, 101*, 462-470.

Lou, S., Li, D. H., Alshaibani, K. A., Xing, H., Li, Z., Huang, Y., & Xia, D. (2022). An all-sky luminance and radiance distribution model for built environment studies.

Renewable Energy, 190, 822-835.

Lou, S., Li, D. H., Lam, J. C., & Lee, E. W. (2016). Estimation of obstructed vertical solar irradiation under the 15 CIE Standard Skies. *Building and Environment, 103*, 123-133.

Moon, P., & Spencer, D. (1942). Illumination from a non-uniform sky. *Illuminating Engineering, 37*, 707-726.

Muneer, T. (2007). *Solar radiation and daylight models*: Routledge.

Norton, B. (2012). *Solar energy thermal technology*: Springer Science & Business Media.

Perez, R., Seals, R., & Michalsky, J. (1993). All-weather model for sky luminance distribution—preliminary configuration and validation. *Solar energy, 50*(3), 235-245.

Soler, A., & Gopinathan, K. K. (2004). Modeling zenith luminance on Madrid partly cloudy skies from diffuse illuminance on a horizontal surface and solar altitude. *Energy Conversion and Management, 45*(15-16), 2591-2601.

Tiwari, G., Tiwari, A., & Shyam. (2016). Handbook of solar energy. In *Handbook of solar energy*: Springer.

Tohsing, K., Klomkliang, W., Masiri, I., & Janjai, S. (2017). *An investigation of sky radiance from the measurement at a tropical site*. Paper presented at the AIP Conference Proceedings.

Torres, J., García, A., De Blas, M., Gracia, A., & Illanes, R. (2010). A study of zenith radiance in Pamplona under different sky conditions. *Renewable Energy, 35*(4), 830-838.

Tregenza, P. R. (1987). Subdivision of the sky hemisphere for luminance measurements. *Lighting Research & Technology, 19*(1), 13-14.

Yao, W., Song, M., Huang, Y., Xu, P., Li, X., Su, G., & Gao, W. (2024). A new anisotropic solar radiation model based on the principle of photothermal integration. *Renewable Energy, 226*, 120436.

มหาวิทยาลัยศิลปากร

VITA

NAME Mr. Worapan Kanchanachat

PUBLICATION

Choosri, P., Nabnean, S., Kanchanachat W., & Teansri, S. (2021). Development of a model and forecasting of hourly UV index using artificial neural network (ANN) at Songkhla. RMUTP Research Journal Sciences and Technology, 15(2), 75-87.

Kanchanachat, W., Masiri, I., & Janjai, S. (2023). Analysis of Zenith Sky Radiance in the Tropics: A case study of Chiang Mai and Nakhon Pathom, Thailand. Current Applied Science and Technology, e0262957-e0262957.

Kanchanachat, W., Masiri, I., Pattarapanitchai, S., Wattan, R., Tohsing, K., & Janjai, S. (2025). A model for calculating relative sky radiance under all sky conditions using geostationary satellite data. Renewable Energy, 251, 123423.

AWARD RECEIVED Good Oral Presentation Award for Classifying CIE standard sky types based on clearness index in central Thailand, The 16th Science Research Conference, Mahasarakham University, February 2025.